

Possibilities and limitations of the sequential kinematic method for simulating evolutionary plasticity problems

Zhenhao Shi^{a,b,*}, Maosong Huang^{a,b}, James P. Hambleton^c

^a*Key Laboratory of Geotechnical and Underground Engineering of Ministry of Education, Tongji University, Shanghai 200092, China*

^b*Department of Geotechnical Engineering, Tongji University, Shanghai 200092, China*

^c*Department of Civil and Environmental Engineering, Northwestern University, Evanston, United States*

Abstract

Evolutionary plasticity processes, such as ploughing and penetrating, widely exist in many geotechnical engineering applications. The simulation of these processes poses considerable challenges due to the occurrence of large deformation, unsteady nature of the material free surface, and inherent coupling between mechanical response and material geometries. This paper explores the possibility of simulating the first-order response of these processes by using sequential kinematic method (SKM) in combination with simple deformation mechanism. The mechanism consists of rigid elements separated by velocity discontinuities. Computations based on the kinematic approach of limit analysis are sequentially performed to evaluate the most likely deformation mode and update material geometries. An r -adaptive kinematic formulation is used that captures versatile velocity fields by optimizing the geometries of simple kinematic mechanism. The modeling methodology is studied in detail for two archetypal evolutionary plasticity problems: wedge

*Corresponding author. Address: Department of Geotechnical Engineering, Tongji University, 1239 Siping Road, Shanghai 200092, China

Email address: 1018tjzhenhao@tongji.edu.cn (Zhenhao Shi)

ploughing Tresca material and cylinder penetrating undrained clay. The numerical results obtained by using the SKM are compared against existing analytical and numerical solutions, as well as experimental evidence. The paper demonstrates that evolutionary plasticity problems can be simulated in a conceptually simple way using SKM and highlights the potential pitfalls of this technique.

Keywords: plasticity, large deformation, limit analysis, kinematic method, *r*-adaptivity

1. Introduction

Evolutionary plasticity processes are ubiquitous in geotechnical engineering problems. As an archetypal example, the process of cutting in dry sand emphasizes the essential characteristics of this type of problems (see Fig. 1). They include continuous failure of materials, large deformation, and significant changes in the material free surface. Similar phenomena have been observed from lateral buckling of seabed pipelines (Tian and Cassidy, 2010; White and Dingle, 2011), soil cutting and tillage (McKyes, 1985; Godwin and O’Dogherty, 2007), and locomotion of legged robots and vehicle mobility (Li et al., 2013; Recuero et al., 2017; Agarwal et al., 2019). From a theoretical viewpoint, modeling evolutionary plasticity processes poses considerable challenges due to nonlinearities introduced by large deformation, material plasticity, and contact interactions.

Simple analytical models have been proposed to tackle the problems by considering particular *states* within the entire deformation *processes*, mostly corresponding to the incipient failure and steady state. The first type of these models is developed within the context of tribology as a means to explain the role of asperities in frictional interactions between surfaces undergoing relative motion

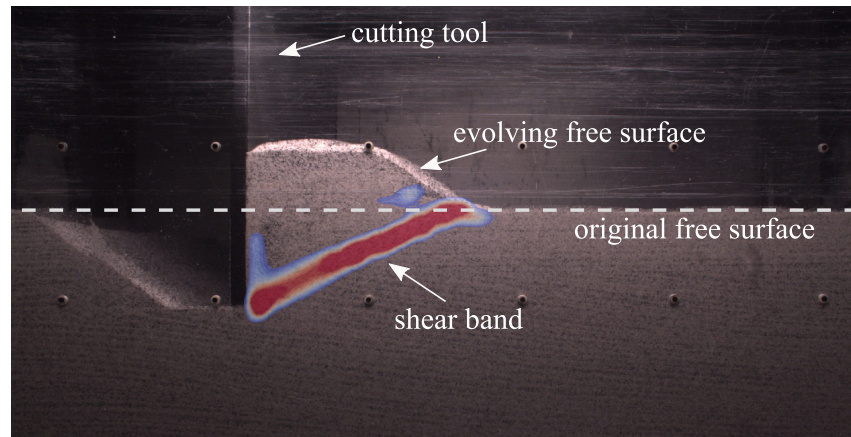


Fig. 1. Deformation pattern and evolution of the material free surface in ploughing a dry sand (Kashizadeh, 2017). Contours show the intensity of the incremental shear strain interpreted by the PIV analyses (White and Take, 2002; Stanier and White, 2013), with the cooler and warmer colors indicating smaller and larger magnitudes, respectively.

18 (Collins, 1972; Challen and Oxley, 1979; De Vathaire et al., 1981; Petryk, 1983).
 19 These models focus on the steady-state motion characterized by invariant resis-
 20 tance and material surface geometry. The second group of models is developed as
 21 tools to predict the loads acting on tillage implements or geotechnical structures
 22 (Osman, 1964; Hettiaratchi and Reece, 1974; Perumpral et al., 1983; Godwin
 23 and O'Dogherty, 2007). Compared with the former group, these models are
 24 mainly interested in the forces required to initiate deformation. When interest is
 25 in simulating the complete deformation processes, numerical methods are nor-
 26 mally required. For this purpose, various numerical techniques have been used
 27 such as large deformation finite element analysis (Bil et al., 2004; Hambleton and
 28 Drescher, 2009; Zhang et al., 2015; Ducobu et al., 2016; Zhang et al., 2020; Zhu
 29 et al., 2020), discrete element method (Hryciw et al., 1997; Tsuji et al., 2012),
 30 and meshfree methods (Leon Bal et al., 2018; Agarwal et al., 2019; Afrasiabi

31 [et al., 2019](#)). These approaches achieve considerable success in handling large
32 deformation and the evolving material free surface but tend to be computationally
33 onerous and overly demanding for routine engineering practice.

34 The sequential kinematic method (SKM) represents a compelling alternative
35 strategy for modeling evolutionary plasticity processes due to its computational
36 efficiency and stability. The technique regards a deformation process as a sequence
37 of failure states, and in each state, the kinematic theorem of limit analysis ([Drucker](#)
38 [et al., 1952](#)) is applied to compute an optimal velocity field that is subsequently
39 used to update the material geometries. The computational efficiency and stability
40 of SKM has been illustrated in different engineering problems such as structural
41 collapse ([Yang, 1993](#); [Corradi and Panzeri, 2004](#)), metal forming ([Hwan, 1997](#);
42 [Raithatha and Duncan, 2009](#)), structural geology ([Cubas et al., 2008](#); [Mary et al.,](#)
43 [2013](#)), and the simulation of penetration, ploughing, and cutting processes in
44 soils ([Hambleton, 2010](#); [Hambleton and Drescher, 2012](#); [Hambleton et al., 2014](#);
45 [Kashizadeh et al., 2015](#); [Kong, 2015](#); [Kong et al., 2018](#); [Zhu et al., 2020](#)). Existing
46 SKM formulations evaluate deformations of the entire computational domain.
47 However, in many problems with engineering relevance, the induced deformation
48 tends to be confined to local regions adjacent to the moving object. In the example
49 depicted in [Fig. 1](#), strains are locally concentrated into a single shear band, and the
50 majority of the bulk materials mainly remains stationary or undergoes rigid body
51 motion. Therefore, the SKM formulation that accounts for the deformation within
52 the entire material domain can be unnecessarily complex and computationally
53 inefficient, especially when the primary interest is a quick prediction of the first-
54 order response such as the forces and motion of the moving object.

55 This paper explores the possibilities of performing a first-order analysis for

56 evolutionary plasticity problems by utilizing SKM in combination with simple
57 kinematic mechanism. In the proposed approach, only deformation adjacent to the
58 moving object is considered and represented by mechanism consisting of sliding
59 rigid elements separated by velocity discontinuities. To allow for versatile veloc-
60 ity fields, the model incorporates an r -adaptive kinematic method operating on
61 the simple mechanism (Shi and Hambleton, 2020). Rather than discretizing the
62 entire domain, the model relies on discretizing solely the material free surface.
63 The modeling methodology is examined for two evolutionary plasticity problems:
64 wedge ploughing Tresca material and cylinder penetrating undrained clay. The
65 simplicity of these problems is appealing from a fundamental perspective, and
66 well-documented experimental observations, as well as analytical and numeri-
67 cal solutions, enable a detailed assessment of the strength and weakness of the
68 proposed technique.

69 **2. General modeling strategy**

70 We employ the problem of wedge ploughing as an archetypal example for
71 conveying the bases of the proposed SKM technique. An object (here a rigid
72 wedge) is pushed into a Tresca solid (Fig. 2(a)), followed by a lateral movement
73 that continuously deforms the cohesive material (Fig. 2(b)). We generally are
74 interested in the forces acting on the moving object (i.e., N and T in Fig. 2)
75 and/or its trajectory. This benchmark problem contains mechanical features that
76 are common to other evolutionary plasticity processes (e.g., see Fig. 2(c) and
77 (d)). First, the material deformed and displaced by the wedge accumulate along
78 the front flank that leads to changes in the free surface (see Fig. 2(b)), alters the
79 deformation patterns of the plastic solid and eventually the resulting forces on the

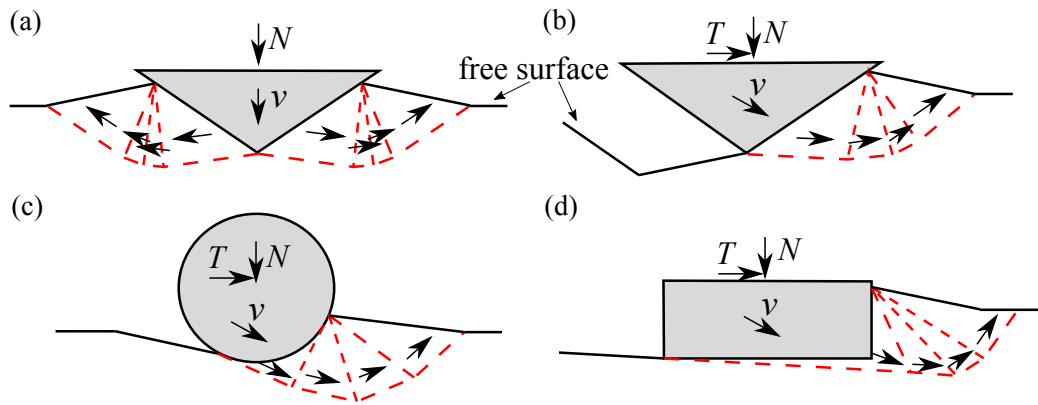


Fig. 2. Schematic illustrating (a) penetrating a plastic solid by a rigid wedge and (b) subsequent ploughing process; (c) ploughing process with circular and (d) rectangular tools.

80 wedge. Second, the contact conditions between the wedge and its surrounding
 81 material evolve as the ploughing proceeds. The interface at the rear flank initially
 82 remains in sliding contact up to a breakpoint where separation suddenly occurs (see
 83 Fig. 2(b)). Our general strategies to tackle these challenges by utilizing SKM are
 84 summarized in the following. These modeling strategies can be extended to other
 85 problems, as illustrated by the later example of cylinder penetration in undrained
 86 clay.

87 As shown in Fig. 3, we describe the velocity fields of the materials surrounding
 88 the wedge by an assembly of rigid elements that only translate in space. The
 89 edges of these elements represent velocity discontinuities. The ploughing process
 90 can then be simulated by sequentially applying the kinematic theorem of limit
 91 analysis based on the rigid element mechanism, and updating material geometries
 92 in accordance with the computed optimal velocity fields (e.g., v_1 to v_4 in Fig. 3).
 93 In general, the mechanisms could be more complex (e.g., including deformable
 94 elements and discretizing entire material domain, see Kong et al. (2018); Zhu

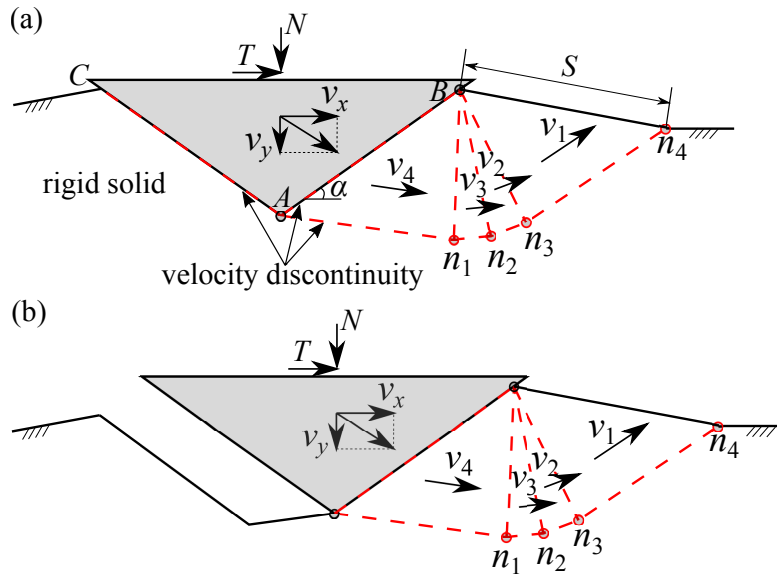


Fig. 3. Schematic illustrating deformation mechanism: (a) during initial wedge ploughing, there are solid-tool interfaces at both front and rear flanks of the wedge; (b) after detaching from solid, there is no interface at the rear flank.

95 [et al. \(2020\)](#)). Nevertheless, the rigid element mechanism reduces the number of
 96 unknowns required to constrain velocity fields and is consistent with the patterns of
 97 concentrated deformation revealed in many evolutionary plasticity processes (e.g.,
 98 see Fig. 1 or those shown by [White and Dingle \(2011\)](#), [Xu and Zhang \(2019\)](#)).

99 Specifically, Fig. 3(a) and (b) depict the mechanisms pertaining to the cases
 100 where the rear flank of the wedge (i.e., AC in Fig. 3) is in contact with the Tresca
 101 solid and has been detached from its neighboring material, respectively. In light
 102 of experimental observation (e.g., [Challen et al. \(1984\)](#)), this work postulates that
 103 the material adjacent to the rear flank of the wedge is rigid during ploughing.
 104 Accordingly, the cases depicted in Fig. 3(a) and (b) can be described by the same
 105 rigid block mechanism, except that the edge AC is treated as an interface (i.e.,

106 velocity discontinuity) in the former case. The aforementioned simplification is
107 made to retain the simplest form of the solution (e.g., less blocks in the mechanism)
108 such that the most clarity on the possibilities and limitations of SKM can be
109 obtained. Indeed, there is no difficulty in adopting a more complex mechanism
110 that would allow for deformation within the material at both sides of the wedge. In
111 fact, our preliminary studies show that both simplified and complex mechanisms
112 yield the same results and in the latter case practically zero-valued velocities are
113 computed for the material adjacent to the rear flank of the wedge.

114 Two types of control can be included in typical SKM modeling: velocity and
115 force control. Under the former condition (also the common working mode), the
116 tool velocities are prescribed, while the forces acting on the tool and material
117 velocity fields are computed from the kinematic theorem. Differently, under the
118 force control, the forces applied on the tool are specified, while the induced tool
119 displacements and evolution of material geometries are sought. Note that the
120 latter control mode can involve iterative processes, where the velocity control is
121 executed for different trial displacements until the force boundary is satisfied. It is
122 also possible to jointly control force and velocity for different degrees of freedom
123 of the object (i.e., mixed control). For the wedge ploughing example, the vertical
124 force acting on the tool (i.e., N in Fig. 3) and its horizontal velocity (i.e., v_x
125 in Fig. 3) can be prescribed, while the vertical velocity (i.e., v_y in Fig. 3) and
126 horizontal force (i.e., T in Fig. 3) are recovered as part of the solution.

127 To actually solve the problem, we have made the following specific assump-
128 tions. The plastic solid is assumed to be weightless, rigid-perfectly-plastic, and
129 obeys the Tresca yield criterion and an associative flow rule. Although this con-
130 stitutive relation is originally used for metals, it has been shown to reasonably

131 approximate the mechanical behavior of cohesive soils (e.g. undrained clay) (Ran-
132 dolph and Houlsby, 1984; Einav and Randolph, 2005; Kong et al., 2018; Zhu et al.,
133 2020). Deformation is considered to be under plane strain conditions. Regard-
134 ing the wedge ploughing example, this assumption applies to the cases where the
135 out-of-plane dimension of the wedge is much larger than the penetration depth.

136 In the following sections, detailed formulation of the SKM will be presented.
137 Specifically, Section 3 discusses the r -adaptive kinematic method that is used to
138 construct optimal velocity fields in combination with rigid block mechanism. The
139 approach to update the material geometries based on computed velocity fields will
140 be presented in Section 4.

141 3. Formulation of r -adaptive kinematic method

142 In this section, we will discuss, for the kinematic mechanism depicted in
143 Figure 3, how an optimal velocity field and the corresponding forces acting on
144 the wedge can be obtained by utilizing the r -adaptive kinematic method. The
145 velocity field of Fig. 3 is constrained by two types of information: the geometries
146 of the rigid elements and their velocities. In r -adaptive kinematic methods, both
147 block velocities and their nodal positions are treated as variables subjected to
148 optimization (Johnson, 1995; Milani and Lourenço, 2009; Hambleton and Sloan,
149 2013). For this purpose, the proposed model constructs a nested optimization
150 procedure that in the inner level determines the optimal velocities for a *fixed*
151 mesh by second-order cone programming (SOCP), and at its outer level computes
152 an optimal set among *variable* nodal positions using non-linear optimization.
153 Respectively, these two optimization layers are detailed in sections 3.1 and 3.2.
154 This r -adaptive kinematic formulation closely resembles that described by Shi

155 [and Hambleton \(2020\)](#) for computing limit states of three-dimensional plasticity
156 problems with fixed material geometries.

157 *3.1. Optimization of velocity field for fixed mesh*

158 For a velocity field characterized by rigid elements, the total energy dissipation
159 rate equals to the sum of those occurring at element edges (i.e., the velocity
160 discontinuities). The latter, for a perfectly plastic material that obeys the Tresca
161 yield criterion, can be expressed as (cf. [Chen \(1975\)](#)):

$$\dot{d} = cl|\Delta v_t| \quad (1)$$

162 The variable l denotes the length of discontinuity, c is the material cohesion,
163 and Δv_t is the tangential velocity jump along element edge. The absolute value
164 is prescribed so that the dissipated power is always positive, regardless of the
165 shearing direction. For rate-sensitive cohesive material, the cohesion c can vary
166 with strain rates. Nevertheless, within the considered rigid element mechanism,
167 plastic deformation all takes place in infinitesimally thin velocity discontinuities,
168 and accordingly strain rates are indefinite (i.e., infinite) ([Chen, 1975](#)). Different
169 modifications or assumptions can potentially be introduced to overcome this diffi-
170 culty. One possibility is the one that is proposed by [Randolph \(2004\)](#) and [Einav
171 and Randolph \(2005\)](#) to consider rate effects in vane shear and T-bar penetrom-
172 eter test. The general idea is to introduce a thickness for velocity discontinuities
173 such that finite strain rates can be defined. Then, a relationship between mate-
174 rial cohesion and strain rate (e.g., see [Dayal and Allen \(1975\)](#), [Ladd and Foott
175 \(1974\)](#), and [Einav and Randolph \(2005\)](#)) can be included. After including these
176 additional relationships, the energy dissipation rate of Eq. (1) becomes a function
177 of both the magnitude of velocity jump and the aforementioned thickness. This

178 latter geometry might be determined by seeking a minimization of the energy
 179 dissipation rate. For a detailed discussion on the aforementioned approach, we
 180 refer the readers to [Randolph \(2004\)](#) and [Einav and Randolph \(2005\)](#). It should be
 181 emphasized that while the technique discussed above shows promising features,
 182 there are questions that required to be thought through when extending the SKM
 183 in accordance with it. One example is related to velocity jump thickness. It is
 184 not clear whether the thickness for a given velocity jump might vary erratically
 185 and unrealistically between consecutive increments during simulating deformation
 186 process and, therefore, whether additional constraints might need to be enforced.

187 To preserve a linear objective function in the SOCP, $|\Delta v_t|$ in Eq. (1) is replaced
 188 by a dummy variable μ :

$$\begin{aligned} \dot{d} &= cl\mu \\ \mu &\geq \sqrt{(\Delta v_t)^2} \end{aligned} \tag{2}$$

189 The constraint specified in Eq. (2) is in the form of second-order cone (SOC)
 190 constraint, one of the types permitted in SOCP in addition to linear equality and
 191 inequality constraints (cf. [Sturm \(2002\)](#)). Eq. (2) recovers the exact energy
 192 dissipation relation when equality is achieved. For the problems presented in this
 193 paper, this condition is always satisfied. This, as will become readily apparent, is
 194 because that the SOCP is formed such that the dummy variable μ is minimized.
 195 For materials that obey the Tresca yielding criterion and associative flow rule,
 196 a kinematically admissible mechanism does not permit velocity jumps that are
 197 normal to element edges ([Chen, 1975](#)):

$$\Delta v_n = 0 \tag{3}$$

198 In accordance with the kinematic theorem of plasticity ([Drucker et al., 1952](#)),
 199 a bound on limit load can be obtained by equating the rate of energy dissipation \dot{D}

200 computed from a kinematically admissible velocity field to the rate of work due to
 201 external forces \dot{W} constructed based on the same field. Such energy balance, for
 202 the system defined in Fig. 3, can be specified as

$$\dot{W} = T v_x + N v_y = \dot{D} = \sum_{i=1}^{N_E} c l_i \mu_i + \sum_{j=1}^{N_I} c_a l_j \mu_j \quad (4)$$

203 where v_x and v_y denote the velocity of the wedge along x -axis and y -axis, respec-
 204 tively, N_E is the number of velocity discontinuities within plastic materials, and
 205 the subscript i is used to indicate quantities corresponding to the i^{th} discontinuity
 206 edge. The second energy dissipation term in Eq. (4) accounts for those occurring
 207 at the interfaces between the wedge and the plastic solid and thus implying that the
 208 wedge and the cohesive mass are treated as a composite dissipative mechanical
 209 system. The variable N_I is the number of the interface segments. The dissipation
 210 at these interface segments is computed by replacing the cohesion c in Eq. (2) with
 211 the interface strength c_a . Perfectly smooth and rough interfaces are characterized
 212 by $c_a = 0$ and $c_a = c$, respectively. A simple contact search algorithm is used to
 213 determine the range of the interface, where the distance from nodes on the free
 214 surface to the wedge flanks is computed and those with a distance less than a
 215 tolerance (1.5×10^{-2} is employed for all simulations in this paper) are considered
 216 to be in contact with the wedge. Conversely, the separation of the wedge from
 217 neighboring plastic solid is naturally considered once the distance exceeds the
 218 tolerance mentioned above. To enable such no-tension interface, a jump condition
 219 that is slightly different than the one given in Eq. (3) is assigned to the interface
 220 segments:

$$\Delta v_n \geq 0 \quad (5)$$

221 As depicted in Fig. 4(a), the velocity jump at the interface is measured from

222 the wedge to the neighboring plastic material such that a positive value of Δv_n
223 indicates separation. The interface behavior described by jointly using Eqs. (1)
224 and (5) is sketched in Fig. 4(b), which is similar to imposing no-tension conditions
225 with respect to the tractions along the surface of a Tresca solid (i.e., the Type
226 A interface model defined by Herfelt et al. (2021), see Fig. 4(c)), except the
227 following aspect. In the SKM model, the separation at interface (i.e., when the
228 normal stress at interface σ_n equals to zero) is associated with interfacial shear
229 stress that coincides with the interface shear strength (i.e., $\tau = c_a$, see Fig. 4(b)).
230 This is because the dissipation of energy along the interface is computed via the
231 interface strength (i.e., see Eq. (1)). Differently, the type A interface model allows
232 separation that is accompanied by interfacial shear stress lower than its limit (i.e.,
233 $\tau < c_a$, see Fig 4(c)).

234 It is acknowledged that the modeling of no-tension interface is challenging
235 and available common approaches, including the Type A interface, can all involve
236 potential pitfalls (see Herfelt et al. (2021) and Houlsby and Puzrin (1999) for a
237 detailed discussion). Nevertheless, it should be emphasized that Eqs. (1) and (5)
238 provide a practical means to account for the no-tension interface behavior via the
239 types of constraints permitted by the SOCP. Moreover, it should be noted that
240 potential imperfections in modeling interface mainly affect the instance of separa-
241 tion (i.e., one computation increment), after which the interface does not exist
242 anymore and consequently is not included in the computation. On the other hand,
243 more investigations can be required in the future regarding the impacts of different
244 interface modeling assumptions on computed cyclic deformation processes, where
245 many interface separation instances can potentially be involved.

246 By manipulating Eq. (4), we obtain the following optimization problem with

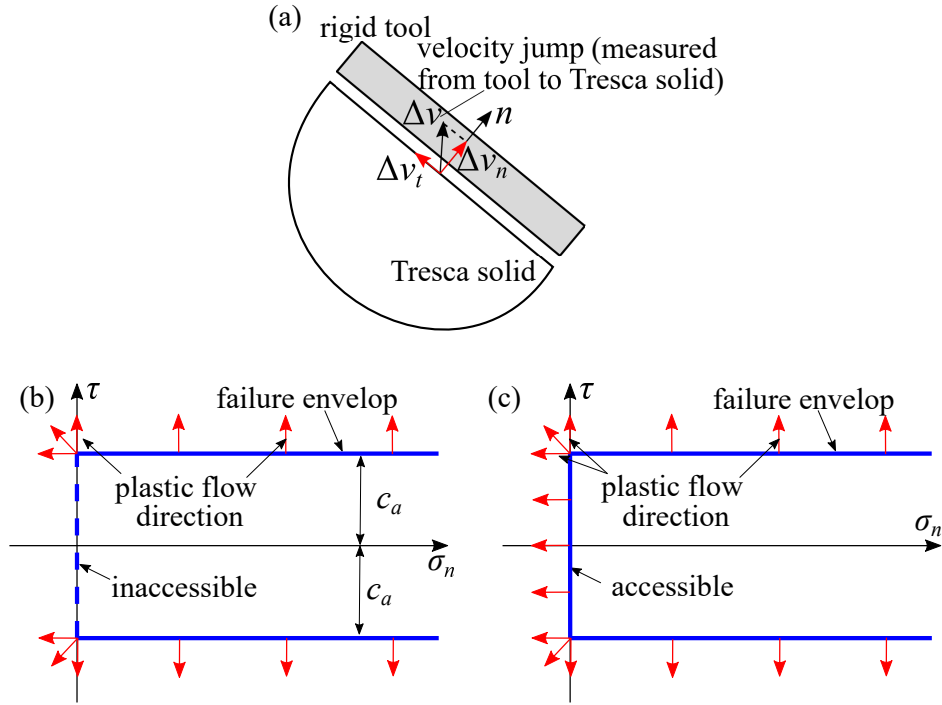


Fig. 4. Schematic illustrating the modeling of non-tension interface between rigid tool and Tresca solid in SKM: (a) interface is treated as velocity jump (measured from tool to Tresca solid); (b) plastic flow directions and failure envelop at the interface; (c) Type A interface model in [Herfelt et al. \(2021\)](#)

247 respect to the velocities of the rigid elements:

$$\min_{v_x} T = \frac{1}{v_x} \left(\sum_{i=1}^{N_E} c l_i \mu_i + \sum_{j=1}^{N_I} c_a l_j \mu_j - N v_y \right)$$

or

$$N = \frac{1}{v_y} \left(\sum_{i=1}^{N_E} c l_i \mu_i + \sum_{j=1}^{N_I} c_a l_j \mu_j - T v_x \right)$$

(6)

$$s.t. \quad \Delta v_{ni} = 0$$

$$\mu_i \geq \sqrt{(\Delta v_{ti})^2} \quad i = 1, \dots, N_E$$

$$\Delta v_{nj} \geq 0$$

$$\mu_j \geq \sqrt{(\Delta v_{tj})^2} \quad j = 1, \dots, N_I$$

248 Equation (6) represents a standard form of SOCP problems and depending on
 249 whether the ploughing or the indentation process is modeled, the first or the
 250 second objective function is employed. The SOCP is solved by the Mosek toolbox
 251 integrated with the MATLAB (Mosek, 2015). N and v_y , T and v_x represent two
 252 work-conjugate pairs. In order to obtain feasible and bounded solutions from the
 253 SOCP, at least one variable in each pair should be specified (e.g., the normal force
 254 N and the horizontal velocity v_x are usually the boundary conditions in modeling
 255 the ploughing). As only rate-insensitive materials are considered in this work,
 256 when setting boundary conditions by prescribing v_x or v_y , a velocity of unity is
 257 assigned for convenience.

258 Equation (6) represents the inner layer of the nested optimization and the com-
 259 puted limit loads correspond to the rigid block mechanism with fixed geometries.
 260 The outer layer of the nested optimization, as detailed in the next section, seeks
 261 optimal nodal positions of the elements (i.e., nodes n_1 to n_4 in Fig. 3(a)) that
 262 minimize the limit loads.

263 3.2. Optimization of nodal positions of rigid elements (r adaptivity)

264 To obtain a critical layout of the velocity discontinuities, we construct the
 265 following non-linear optimization problem:

$$\begin{aligned}
 \min \quad & F(x_{ij}, S) \quad i = 1, 2 \quad \text{and} \quad j = 1, 2, 3 \\
 \text{s.t.} \quad & A_k(x_{ij}, S) \geq 0 \quad k = 1, \dots, 4 \\
 & x_{ij}^l \leq x_{ij} \leq x_{ij}^u \\
 & S > 0
 \end{aligned} \tag{7}$$

266 The objective function in Eq. (7) is the limit tangential or normal force computed
 267 for a given set of nodal positions x_{ij} (the first subscript denotes the i^{th} component

268 of the position vector, while the second subscript indicates the j^{th} node), evaluated
269 in precisely the same way as in the previous section. The coordinates of the nodes
270 n_4 in Fig. 3 cannot be regarded as independent unknowns in the optimization since
271 this node has to lie on the material free surface. We implicitly define the location
272 of this node by an auxiliary variable S that measures the distance between the
273 node n_4 and the intersection point of the wedge and the free surface (i.e., the point
274 B in Fig. 3). To prevent the inter-penetration of rigid elements and consequently
275 ensure computational stability, the first set of constraints in Eq. (7) requires that
276 element areas A_k are always positive. The variables x_{ij}^l and x_{ij}^u appearing in
277 the second set of inequality constraints define allowable limits for certain nodal
278 position components. These constraints are set to ensure that the adjusted nodes
279 do not go beyond the material free surface.

280 As the objective function and constraints of Eq. (7) are both non-linear func-
281 tions of the unknown variables, such problem falls within the general domain
282 of non-linear constrained optimization. In preliminary studies, two of the most
283 widely employed algorithms, interior point method and sequential quadratic pro-
284 gramming, are used to solve this optimization through the FMINCON solver of
285 the MATLAB. These initial investigations show that the interior point method can
286 find a solution with fewer iterations and thus are selected for all computations
287 presented in this paper. Three key parameters that can affect the performance of
288 the interior point method are (1) step size factor Δs in finite difference method that
289 determines the perturbation amount of unknown variables for numerically com-
290 puting the gradient of the objective function; (2) step tolerance T_s that specifies
291 the lower bound on the change of the norm of the vector containing all unknown
292 variables; (3) the tolerance for the optimality T_o that measures the proximity of the

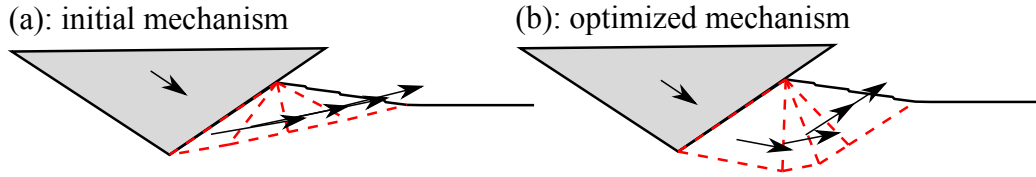


Fig. 5. Typical evolution of kinematic mechanism during r -adaptive kinematic method.

293 current solution to an optimal one. The first parameter affects the accuracy of the
 294 calculated gradient of the objective function, while the latter two mainly influence
 295 the accuracy of the solution as the optimization process will be terminated once
 296 either tolerance is triggered. For simulations performed in this work, we observe
 297 that the solutions are not particularly sensitive to the values of Δs and T_o , and their
 298 default values (i.e., $\Delta s = 1 \times 10^{-6}$ and $T_o = 1 \times 10^{-6}$) are adopted. The parameter
 299 T_s , on the other hand, can noticeably influence the computed response, as it will
 300 be discussed more deeply in the following. For all examples considered in this
 301 work, $T_s = 1 \times 10^{-4}$ to 1×10^{-5} are sufficient. Lastly, it should be noted that the
 302 algorithm used to solve the non-linear optimization is deemed as a local optimizer
 303 and therefore behave most effectively when the initial nodal positions of the rigid
 304 elements (e.g., Fig. 5(a)) are relatively close to optimal ones (e.g., Fig. 5(b)) or the
 305 objective function is convex.

306 **4. Update of material free surface**

307 As shown in Fig. 6(a), deformation of the entire bulk material is tracked
 308 through a discretized free surface. By doing so, the need to repeatedly remesh
 309 the computational domain, as a means to handle severely distorted mesh, can be
 310 avoided. The surface initially has uniform nodal spacing denoted by Δx . The
 311 optimal velocity fields obtained in accordance with the technique discussed in the

312 previous section are used to update the displacements of the nodes along the free
 313 surface by explicit time integration. Consider a pseudo time increment ΔT_n and
 314 let the superscripts $n - 1$ and n denote quantities at the pseudo time T_{n-1} and
 315 T_n ($T_n = T_{n-1} + \Delta T_n$), respectively. With one-step time-marching scheme, nodal
 316 displacements at the end of the increment ΔT_n is found to be:

$$d_{ij}^n = d_{ij}^{n-1} + v_{ij}^{n-1} \Delta T_n \quad i = 1, 2 \quad \text{and} \quad j = 1, 2, \dots \quad (8)$$

317 where d_{ij} and v_{ij} denote the i^{th} component of the displacement and velocity
 318 vectors at the j^{th} node. For nodes belonging to multiple blocks (e.g., the point B
 319 in Fig. 6), an averaged velocities of those blocks are assumed to be nodal velocity
 320 (see Fig. 6(b)). Similarly, the position of the rigid wedge is updated according to

$$d_{iw}^n = d_{iw}^{n-1} + v_{iw}^{n-1} \Delta T_n \quad i = 1, 2 \quad (9)$$

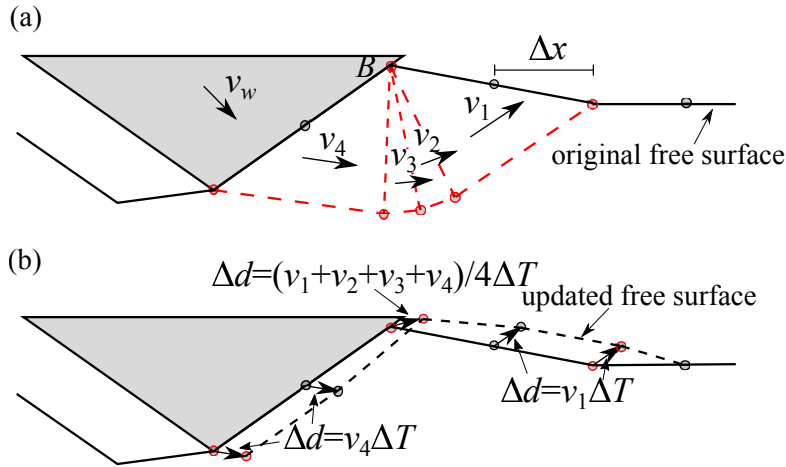


Fig. 6. Schematic illustrating the update of the material free surface according to the computed velocity field: (a) velocity field obtained for geometry configuration at step n ; (b) updated free surface and geometry configuration at step $n + 1$.

321 where d_{iw} and v_{iw} represent the displacement and velocity vectors of the rigid
322 wedge. Once the geometry of the free surface and the position of the wedge have
323 been updated, the contact between the wedge and its neighboring materials is
324 checked based on the searching algorithm discussed in Section 3 and the portions
325 of the material free surface that are in contact with the wedge are treated as velocity
326 discontinuities within the kinematic mechanism.

327 As the size of the time increment is finite, some nodes on the free surface may
328 penetrate the object after the update described above, thus requiring correcting the
329 free surface. Following Kong (2015), those nodes that invade into the interior of
330 the object are mapped back to the boundary of the object along a direction normal
331 to the boundary, as illustrated in Fig. 7(a). Another type of free surface that requires
332 appropriate correction is the sharp inverse corner depicted in Fig. 7(b). Without
333 treatment, the computed boundary between the deforming and stationary materials
334 can be forced to pass the tip of the corner, which represents a local minimum for
335 the objective function (recall that the nature of the selected algorithm is a local
336 optimizer). This behavior prevents searching for better deformation mechanisms,
337 and consequently leads to peculiar jumps on the ploughing resistance and unreal-
338 istic deformation patterns, as will be discussed in the following. To resolve this
339 issue, we loop over all surface nodes and delete those whose x coordinate is less
340 than that of its two neighboring nodes, as suggested by Kong (2015). Figure 7(b),
341 in which the number adjacent to nodes indicates the order of being deleted, shows
342 that by repeatedly checking surface nodes and applying the rule described above,
343 the shape corner can be eliminated. Lastly, it should be noted that the need to
344 correct the surface profile is common to methods that rely on discretization of
345 the entire domain (e.g., finite element limit analysis (Kong, 2015)) as well as the

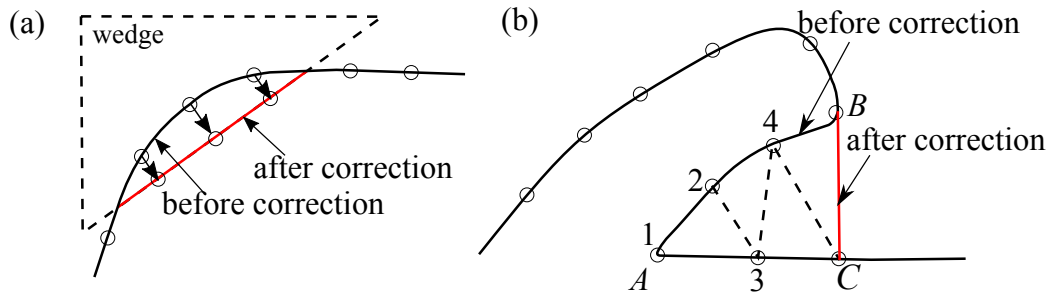


Fig. 7. Schematic illustrating the correction of the material free surface for: (a) penetration into the tool; (b) sharp inverse corner.

346 proposed method.

347 **5. Simulation of smooth wedge indentation and ploughing**

348 The performance of the proposed SKM model is first examined in the case of
 349 indenting and ploughing a Tresca solid by a smooth rigid wedge (i.e., the interface
 350 strength $c_a = 0$). In this example, the wedge angle α (see Fig. 3 for its definition)
 351 equals to 10° , while the material cohesion $c = 13$ MPa. In the simulations, the
 352 wedge is first pushed into the plastic solid, followed by a lateral ploughing with
 353 the normal load maintained at the same level as the one reached at the end of the
 354 indentation. Both indentation and ploughing processes are under velocity control
 355 in the simulations (i.e., the velocity v_x or v_y in Fig. 3(a) is prescribed).

356 Fig. 8 compares the computed indentation resistance with that given by Hill
 357 et al. (1947)'s slip-line solution. A good agreement can be observed. Fig. 9
 358 presents the optimal velocity fields (i.e., deformation mechanisms) when the
 359 intruder penetrates to different depths. These fields exhibit geometrically self-
 360 similarity, which is explicitly assumed in Hill et al. (1947)'s solution but comes
 361 out automatically from the SKM.

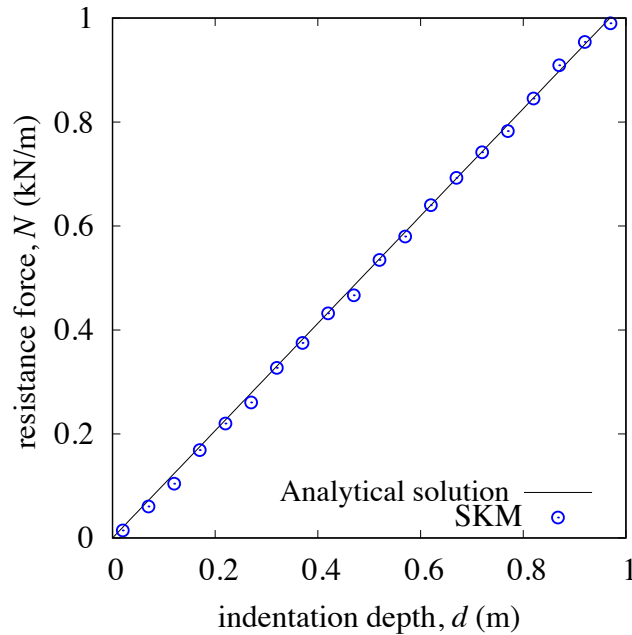


Fig. 8. Comparison between the penetration resistance computed by the SKM and slip-line solution (Hill et al., 1947). Note that the SKM simulation employs nodal spacing $\Delta x = 0.5$ and time increment $\Delta T = 0.05$.

362 Fig. 10 shows the computed trajectory of the wedge as well as the normalized
 363 tangential force during the ploughing stage. The deformation mechanisms for
 364 selected instances are given in Fig. 11. It is seen that the initial lateral ploughing
 365 leads to a sinking of the wedge. This deformation pattern, referred to as “junction
 366 growth” within tribology (Tabor, 1959; Challen and Oxley, 1979), occurs because
 367 the contact pressure on the rear flank is relieved and the wedge penetrates deeper
 368 into the plastic solid to achieve a larger contact area at the front flank to sustain
 369 the applied normal load. As the lateral ploughing continues, the wedge begins to
 370 rise and simultaneously push a bow wave of plastically deformed material ahead
 371 as depicted in Fig. 11(b) and (d). Such rising phase continues until reaching

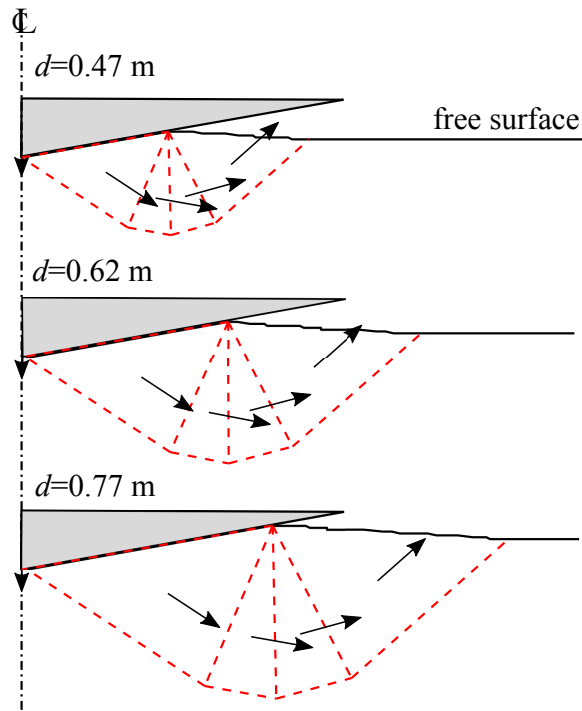


Fig. 9. SKM computed velocity field at various stages of rigid wedge indentation.

372 a steady state characterized by approximately constant ploughing resistance and
 373 wedge vertical location. It is seen that the computed rising trajectory is not smooth
 374 but with small-amplitude oscillations. The latter is attributed to the alternation
 375 between two deformation mechanisms respectively depicted in Fig. 11(c) and (d).
 376 The former mode is characterized by the wedge sliding along its front flank without
 377 deforming the solid, which gradually reduces the contact area between the wedge
 378 and the solid mass. When the contact area is not enough to sustain the applied
 379 normal load, the second mode characterized by a bear-capacity type failure occurs.
 380 The contact area grows consequently.

381 To examine the accuracy of the SKM simulation, two alternative solutions
 382 are included in Fig. 10. Hambleton (2010) proposes a semi-analytical method

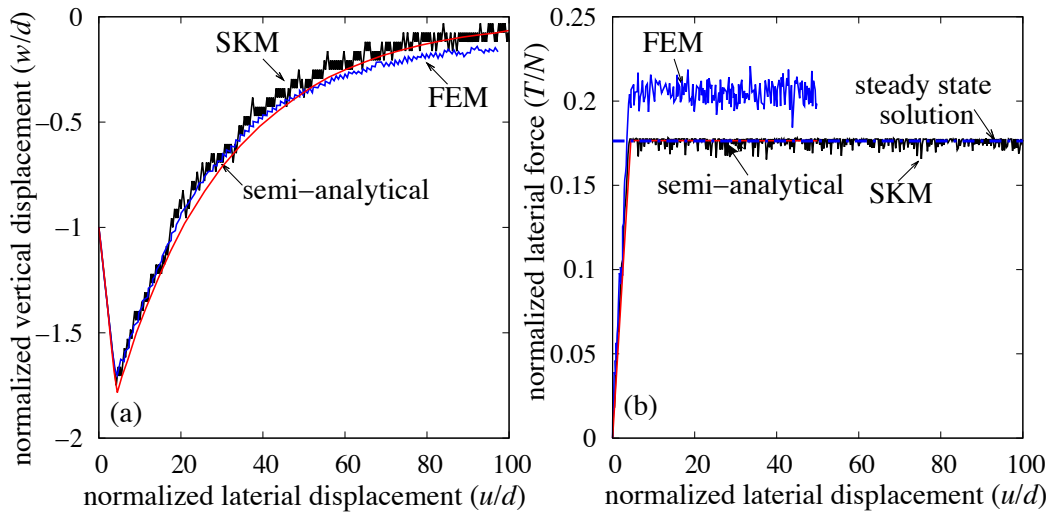


Fig. 10. Comparison between smooth wedge ploughing response computed by the SKM, finite element, semi-analytical method (Hambleton, 2010), and analytical steady-state solution (Challen and Oxley, 1979). Note that the SKM simulation employs nodal spacing $\Delta x = 1$ and time increment $\Delta T = 0.25$.

383 by treating the ploughing as a sequence of incipient plastic flow problems that
 384 can be approximated by Hill et al. (1947)'s indentation mechanism. An FEM
 385 simulation is also performed by Hambleton (2010) to verify the semi-analytical
 386 model. This numerical analysis is conducted by using ABAQUS/Explicit. The
 387 arbitrary Lagrange-Eulerian (ALE) remeshing algorithm is employed in the region
 388 near the wedge to maintain a high-quality mesh after relatively large deformation
 389 has occurred. The rigid-plastic behavior of the solid is emulated by using the
 390 Tresca model with a large value of Young's modulus E (e.g., $E/c \approx 7000$). More
 391 detailed discussions on the features of the FEM can be found in Hambleton and
 392 Drescher (2012, 2009). A good agreement can be seen from these comparisons.
 393 The ploughing force at long distances computed by the SKM and semi-analytical
 394 approach are close to the steady-state solution proposed by Challen and Oxley

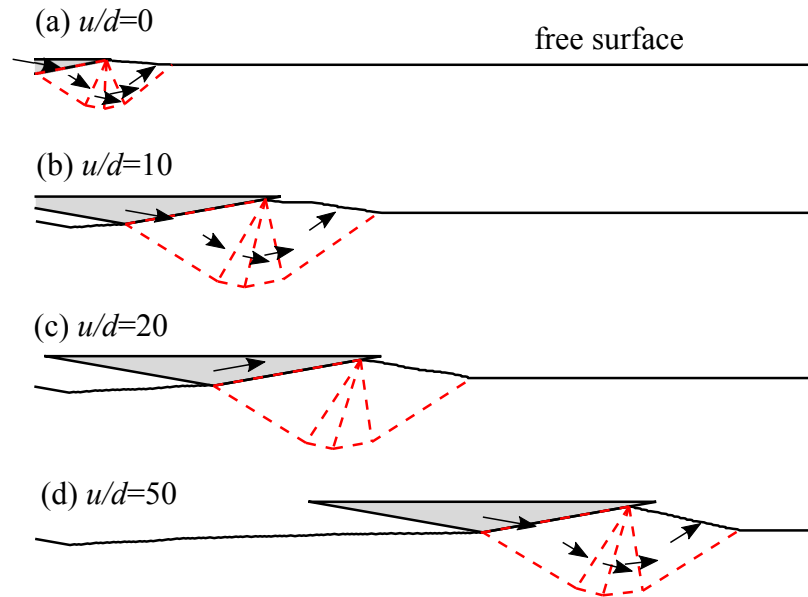


Fig. 11. SKM computed evolution of the material free surface and velocity fields during smooth wedge ploughing.

395 (1979), while the FEM tends to predict a bit higher resistance. Note that the FEM
 396 simulation shows similarly oscillatory wedge trajectory and ploughing resistance,
 397 as computed by the SKM.

398 6. Convergence analysis of SKM simulation

399 We use the ploughing simulation discussed in the previous section as an op-
 400 portunity to evaluate the convergence features of the SKM solution with respect to
 401 the discretization size of the free surface represented by the nodal space, Δx , and
 402 the step size of the time marching represented by the time increment, ΔT .

403 Fig. 12(a) and (b) shows the ploughing simulations performed under three
 404 different time steps. It can be seen that the computed wedge trajectory and
 405 tangential force both show a converging tendency as ΔT decreases. The decrease

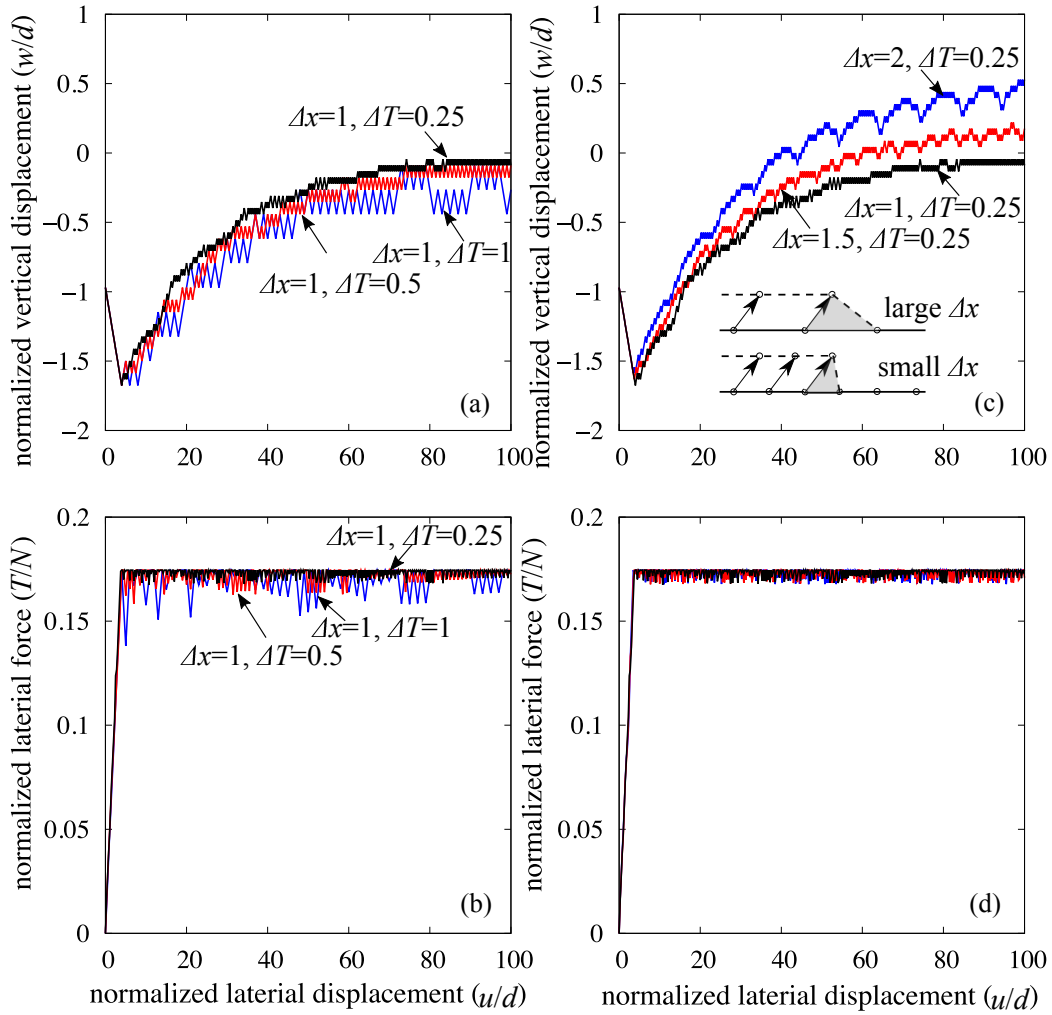


Fig. 12. Convergence analyses of SKM solution with respect to time increment size (subfigures (a) and (b)) and nodal space along the discretized free surface (subfigures (c) and (d)).

406 in the time step also leads to smaller fluctuations in the computed response. The
 407 same convergence feature can be observed for reducing the nodal spacing Δx , as
 408 illustrated in Fig. 12(c) and (d). It is noticed that the simulations based on larger
 409 nodal spaces generate trajectories that elevate to higher positions. Such response
 410 might result from the fact that a linear function is used to interpolate the free

411 surface between adjacent nodes (see the inset of Fig. 12(c)). In this illustration, the
412 solid and dashed lines represent the free surface before and after the update, and
413 the gray area denotes the fictitious material that is added to preserve the continuity
414 of the free surface. Larger nodal space implies more artificial material is piled
415 up ahead of the wedge and consequently the deformation mode associated with
416 wedge upward motion (e.g., that shown in Fig. 11(c)) can be sustained for longer
417 periods. As a consequence, the wedge heads to larger elevations.

418 The aforementioned analyses indicate that the volume conservation for incom-
419 pressible Tresca solid can be violated in SKM simulations, due to the resources
420 like the addition of artificial material mentioned above and the correction of the
421 material free surface discussed in section 4. To assess how this violation is affected
422 by the employed nodal spacing and time increment, the change of material volume
423 in the convergence analysis of Fig. 12 is evaluated (see Table 1). These reported
424 volume changes are computed by numerically integrating the material free surface
425 at the end of the simulations. The data suggest that the change of material volume
426 tends to decrease as smaller time increments are employed (i.e., compare lines
427 1 to 3 of Table 1). On the other hand, when larger nodal spacing is used, more
428 artificial material can be added to computation domain (i.e., compare lines 3 to 5
429 of Table 1), as discussed above.

430 **7. Simulation of rough wedge indentation and ploughing**

431 We have shown that the r -adaptive SKM model can reasonably represent the de-
432 formation processes of a Tresca solid ploughed by a smooth wedge. In this section,
433 we further evaluate this technique in the case of ploughing cohesive solid by wedge
434 where finite adhesion presents at contact surfaces. The experimental observations

Table 1. Change of material volume at the end of ploughing simulations that employ different nodal spacing and time increment (see Fig. 12). Note that the volume change is normalized by the initial volume before ploughing, V_0 . This initial volume corresponds to a rectangular region with a depth twice the wedge indentation depth prior to ploughing d and a length twice the lateral ploughing distance u , i.e., $V_0 = 4du$.

Nodal spacing, Δx	Time increment, ΔT	Change of material volume, $\Delta V/V_0$
1.0	1.0	-7.6 %
1.0	0.5	-3.6 %
1.0	0.25	-2.0 %
1.5	0.25	-1.1 %
2.0	0.25	0.01 %

435 for ploughing aluminum alloy by a hard wedge (Challen et al., 1984) are used to
 436 assess the model in the aforementioned aspect. These tests are chosen because they
 437 provide a rich experiment dataset (i.e., the evolution of ploughing resistance and
 438 tool trajectory) that helps to evaluate the SKM model relatively comprehensively.
 439 Albeit being different materials, the mechanical behavior of metal and cohesive
 440 soil (e.g., undrained clay) is similar in some key aspects such as incompressibility
 441 conditions. Constitutive models and analytical solutions developed originally for
 442 metal have been successfully employed to analyze geotechnical problems (Mroz,
 443 1967; Prévost, 1977; Lemaitre and Chaboche, 1990; Anastasopoulos et al., 2011;
 444 Karapiperis and Gerolymos, 2014; Prandtl, 1920; Terzaghi, 1943). Following this
 445 line of thought, simulating the tests of ploughing metal is expected to provide
 446 a meaningful evaluation of the SKM model regarding its capacity to model the
 447 counterpart geotechnics problems (e.g., ploughing cohesive soil (Hettiaratchi and

Table 2. Parameters in the SKM simulations of the ploughing tests performed by [Challen et al. \(1984\)](#).

Test	α (°)	N (N/mm)	c (MPa)	c_a (MPa)
10	25.9	700	243	26.73
12	35.05	700	200	30
19	10.2	700	193	82.99

448 [Reece, 1974](#); [Palmer, 1999](#); [Atkins, 2009](#)) and the lateral sliding of pipeline in
449 undrained clay ([Tian and Cassidy, 2010](#); [White and Dingle, 2011](#))).

450 Table 2 summarizes the geometric and material parameters used in the simula-
451 tions. The material properties are reported by [Challen et al. \(1984\)](#) except that for
452 the test 12, which is not available from the literature. This information is estimated
453 in this study by fitting the ploughing force at long distances. In the simulations, an
454 indentation stage is modeled prior to the ploughing, which ceases when the normal
455 forces applied in the experiments (see Table 2) are reached. Due to the lack of
456 experimental data, a comparison between the computed and measured evolution of
457 the penetration resistance with the indentation depth is not available. Nevertheless,
458 the comparison between the calculated and measured wedge tip elevation at the
459 beginning of the ploughing (see Figs. 13, 14 and 15) suggests that the indentation
460 stage is reasonably represented by the model.

461 Comparisons of full force-displacement histories for the three ploughing tests
462 are shown in Figs. 13, 14 and 15. In general, a good agreement can be seen
463 between the computed and observed response. The calculated ploughing forces at
464 long distances and the corresponding velocity fields (see Fig. 16) can be considered
465 consistent with the steady-state solution proposed by [Challen and Oxley \(1979\)](#).

466 Nevertheless, strictly speaking, steady state (i.e., invariant ploughing resistance
467 and wedge depth) is not reached in the SKM simulations. It is conjectured that
468 this response might be attributed to the following resources. The numerical
469 simulations of the whole evolutionary process as described in this work can be
470 influenced by factors like the errors due to space and time discretization and their
471 accumulation. These variables can make it hard to recover steady-state solutions
472 that are constructed to satisfy specific conditions. The aforementioned numerical
473 errors might partially be reflected by the fact that the computed ploughing force
474 at long distances in different tests displays different degree of approximation with
475 respect to [Challen and Oxley \(1979\)](#)'s solution. The other possible reason is
476 the non-uniqueness in steady-state solutions as argued by [Hill \(1950\)](#), [Collins
477 \(1972\)](#), and [Petryk \(1980\)](#). The SKM simulations might eventually switch between
478 different steady-state configurations, and thus a strictly defined steady state is not
479 reached.

480 Other quantitative mismatches between model simulations and test data can
481 also be observed. For example, the simulations show that there is a sudden drop
482 of tangential force once the wedge starts to rise (see Fig. 14), resulting from the
483 separation at the rear flank of the wedge and the consequent loss of resistance
484 related to the interface strength. This feature is not observed from test results,
485 where the separation may be a progressive process and thus leading to a smooth
486 change of the ploughing resistance. Remarkable hardening and softening stages
487 are observed from the experimental data of the test 19, which are not captured
488 by the model possibly due to the underlying assumption that the solid is perfectly
489 plastic.

490 The computation times (total runtime) and the number of Mosek calls for the

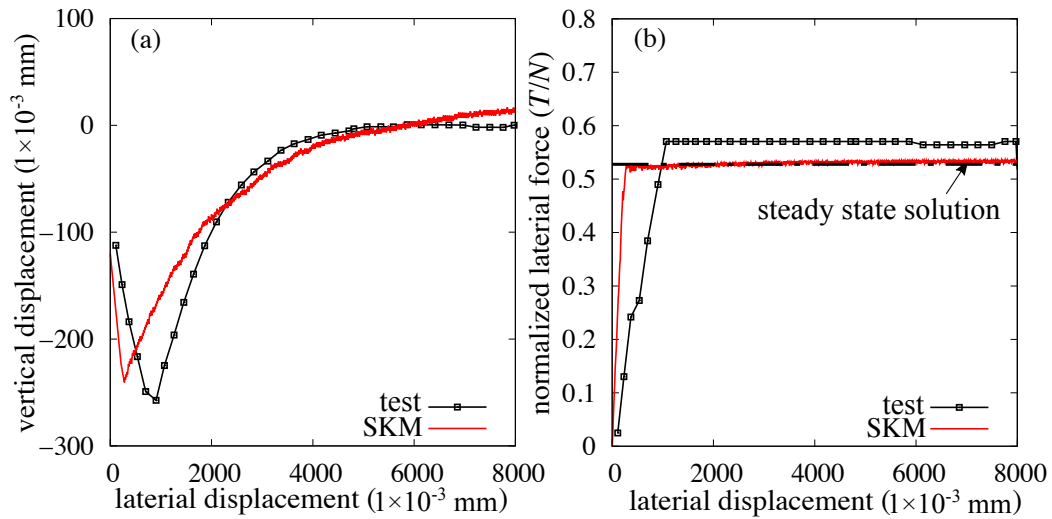


Fig. 13. Comparison between SKM simulated ploughing response, experimental data (test 10 in Challen et al. (1984)) and analytical steady-state solution (Challen and Oxley, 1979). Note that the SKM simulation employs nodal spacing $\Delta x = 60$ and time increment $\Delta T = 10$.

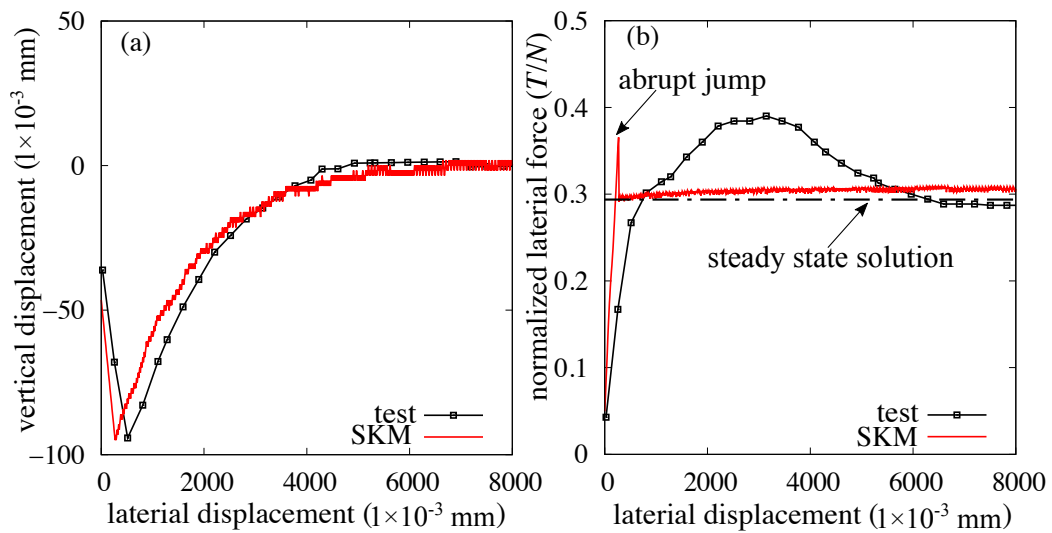


Fig. 14. Comparison between SKM simulated ploughing response, experimental data (test 19 in Challen et al. (1984)) and analytical steady-state solution (Challen and Oxley, 1979). Note that the SKM simulation employs nodal spacing $\Delta x = 60$ and time increment $\Delta T = 10$.

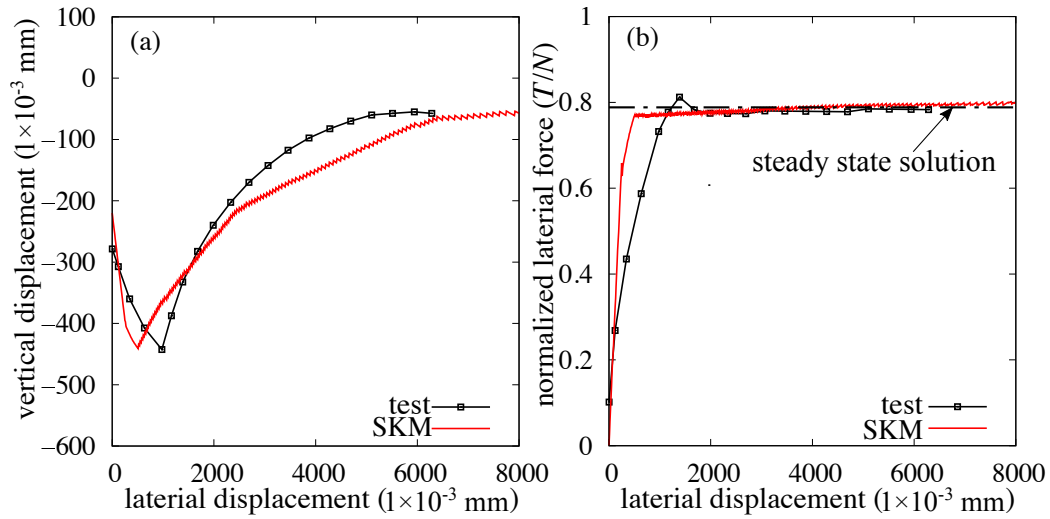


Fig. 15. Comparison between SKM simulated ploughing response, experimental data (test 12 in Challen et al. (1984)) and analytical steady-state solution (Challen and Oxley, 1979). Note that the SKM simulation employs nodal spacing $\Delta x = 60$ and time increment $\Delta T = 10$.

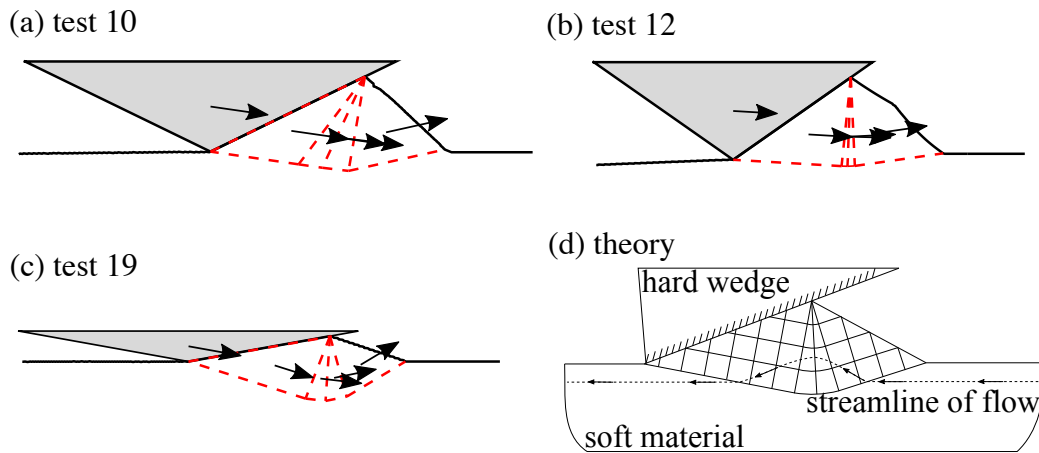


Fig. 16. Comparison between SKM computed velocity fields at long distances and that postulated in the steady-state solution (reproduced from Challen and Oxley (1979)).

491 simulations described above are summarized in Table 3. It is seen that the cost
 492 of using r -adaptive SKM for simulating large deformation processes is relatively

493 small. The runtime can potentially be brought down further via the implementation
 494 of Mosek through platforms that require smaller overhead than the MATLAB. The
 495 fact that the simulation of the test 12 consumes the largest cost is because a
 496 smaller value of the parameter T_s (see section 3.2 for its definition) is employed
 497 to ensure the solution accuracy and consequently more iterations are conducted in
 498 the non-linear optimization of Eq. (7).

499 8. Simulation of cylinder penetration in undrained clay

500 To illustrate the application of the proposed SKM to other evolutionary plastic-
 501 ity problems in geotechnical engineering, plain-strain cylinder penetrating undrained
 502 clay is simulated in the following. This deformation process is similar to that taking
 503 place during the T-bar penetrometer test widely used in geotechnical site charac-
 504 terization (Einav and Randolph, 2005). Normally, the longitudinal dimension of
 505 the penetrometer is much greater than its in-plane ones, and thus the plain-strain
 506 conditions can be reasonably adopted.

507 Figure 17 shows the kinematic mechanism used in the SKM simulations. Con-

Table 3. Computation times (unit:second) and Mosek calls for SKM simulations of lateral ploughing. Note that the reported times are total runtime on a PC equipped with an Intel i9-9900 processor (3.6 GHz; 8 cores) and 32 GB RAM. Test numbers in the table refer to those performed by Challen et al. (1984).

Cases	Total runtime	Number of Mosek calls
Test 10	251	19624
Test 12	900	97071
Test 19	241	23545

508 sidering the symmetry of the problem, only half of the domain is modeled. The
509 T-bar penetrometer with a diameter of D is approximated by a rigid polygon (see
510 Fig. 17(a)) that allows treating the soil-tool interfaces as planar velocity discontinuities.
511 As the penetration proceeds, the SKM adds new blocks to kinematic
512 mechanism to facilitate the growth in the soil-tool contact region. Specifically, a
513 new pair of rigid blocks are included when a new polygon edge becomes in contact
514 with the soil free surface (e.g., BC in Fig. 17(b)). To ease the comparison between
515 the SKM simulations and existing solutions, the following settings are specified.
516 The shear strength of undrained clay S_u distributes uniformly along depths. The
517 Tresca solid is used to approximate undrained clay, i.e., cohesion c in Eq. (1)
518 equals to S_u . The soil-tool interface features a strength of $c_a = S_u/2$. Other model
519 settings are the same as those employed in the aforementioned wedge ploughing
520 example. Lastly, the simulations are performed by prescribing the velocity of the
521 T-bar (i.e., v_y in Fig. 17).

522 Figure 18 shows the computed variation of penetration resistance with depths
523 by the SKM and finite element method (FEM) (Zhu et al., 2020). In the FEM
524 simulation, Coupled Eulerian-Lagrangian (CEL) technique is used to handle the
525 large deformation of soil. Similar to the SKM model, the Tresca model is used
526 to describe the behavior of undrained clay. More detailed discussions on the
527 features of the FEM modeling can be found from Kong (2015), Kong et al. (2018),
528 and Zhu et al. (2020). The results given by the two numerical approaches agree
529 reasonably, and show a consistent trend that the penetration resistance grows
530 at smaller rates as the depth increases. The analytical solutions proposed by
531 Hambleton and Drescher (2012) and Martin and Randolph (2006), applicable
532 respectively to cylinder shallow and deep penetration, are included in Fig. 18. In

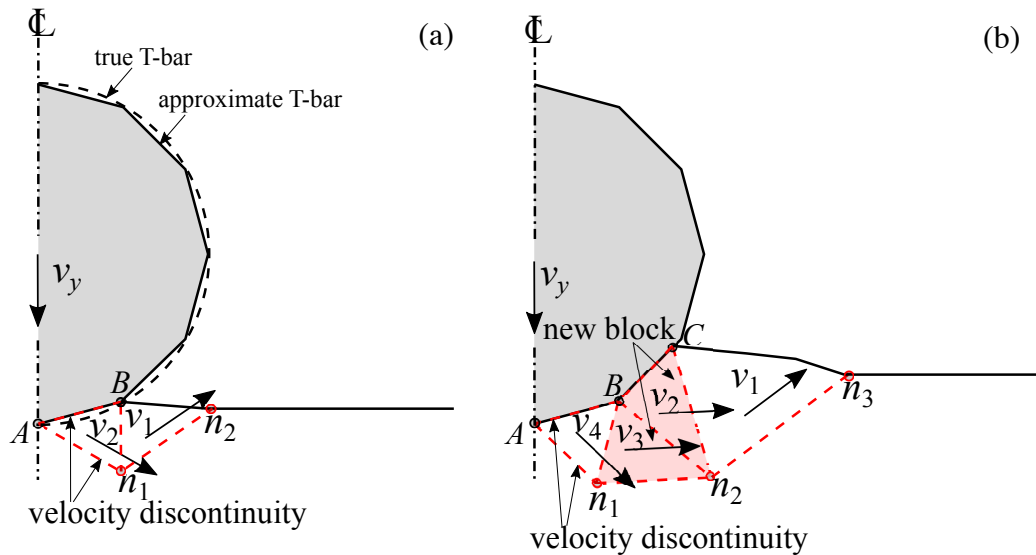


Fig. 17. Kinematic mechanism in the simulation of rigid cylinder penetration: (a) early contact; (b) new blocks are added to facilitate the growth in soil-tool contact area.

533 the former work, a closed-form solution for cylinder indentation is constructed
 534 by examining the asymptotic state of evolutionary processes characterized by the
 535 Prandtl-type punch mechanism (Hambleton and Drescher, 2012). The latter study
 536 presents an upper bound solution for a cylindrical plane-strain object translating
 537 through a rigid plastic solid (Martin and Randolph, 2006). Figure 18 shows that
 538 the force-penetration relationship computed by the SKM matches reasonably with
 539 the solution of Hambleton and Drescher (2012) at shallow depths and approaches
 540 to the solution of Martin and Randolph (2006) at deep locations.

541 The change in the free surface and deformation mechanism of soil as the
 542 penetration proceeds is presented in Fig. 19. These patterns of evolving material
 543 geometries are consistent with those revealed from FEM simulations (Kong et al.,
 544 2017; Zhu et al., 2020). Note that, for deep penetration (see Fig. 19(c)), the SKM
 545 computes surface failure mechanism (i.e., the flow of soil extends to the ground

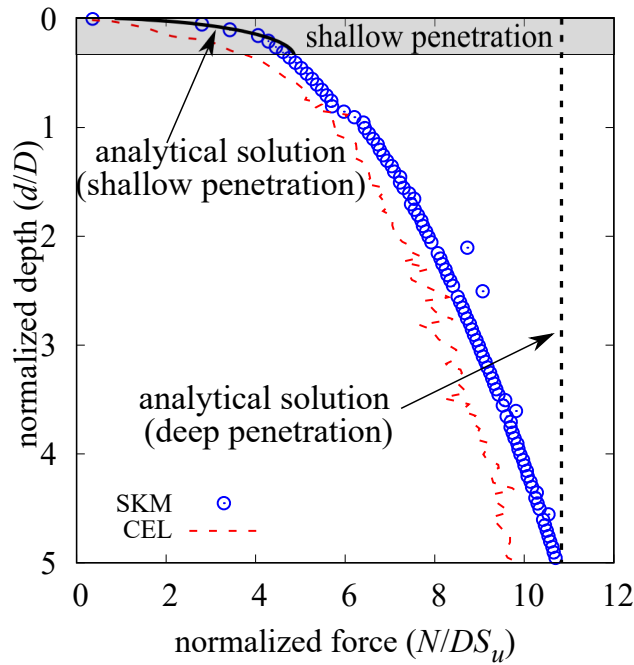


Fig. 18. Force-displacement relationship during cylinder penetration process computed by the SKM, Coupled Eulerian-Lagrangian (CEL) finite element method, and analytical models. Note that the SKM simulation employs nodal spacing $\Delta x = 0.01$ and time increment $\Delta T = 0.02$. The analytical solution for shallow penetration is described in [Hambleton and Drescher \(2012\)](#), while that for deep penetration is given by [Martin and Randolph \(2006\)](#).

546 surface) rather than full-flow mechanism as seen in the upper bound solution
 547 of [Martin and Randolph \(2006\)](#), albeit that the magnitude of soil velocities at
 548 shallow depths is noticeably reduced. The reasons behind such discrepancy will
 549 be discussed in the following section.

550 9. Possibilities and limitations of SKM

551 We have shown that how two archetypal problems of evolutionary plasticity
 552 processes (wedge ploughing and cylinder penetration) can be modeled by the SKM

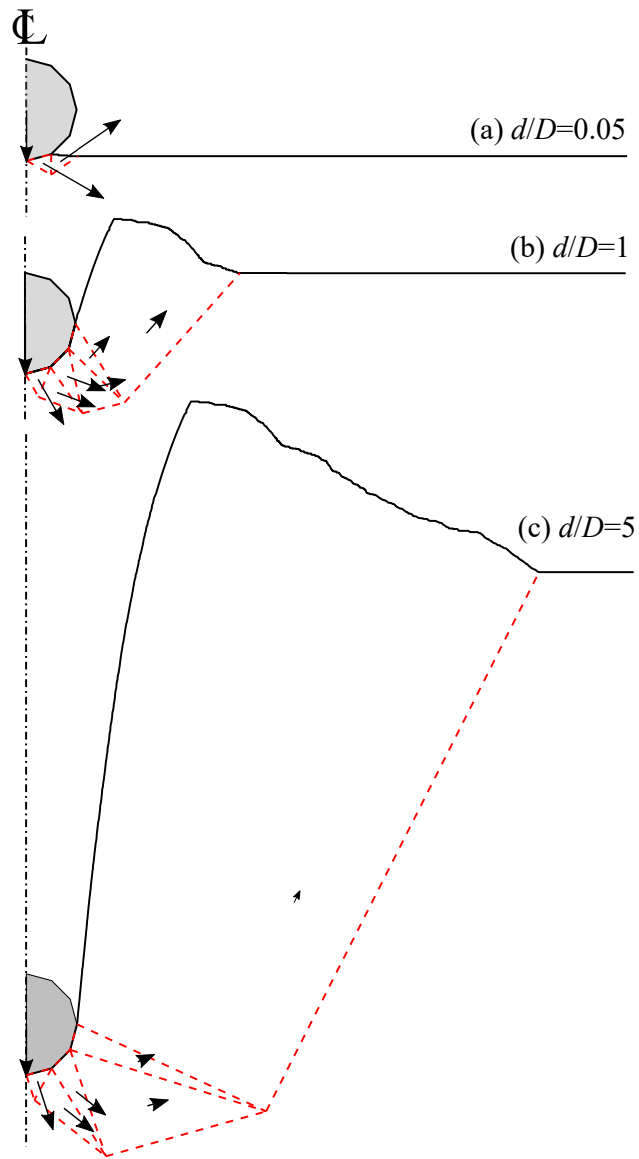


Fig. 19. Material free surface and soil deformation mechanism computed by the SKM that correspond to different cylinder penetration depths.

553 in combination with simple kinematic mechanism. By comparing against analyti-
 554 cal and numerical solutions as well as experimental evidence in the literature, we

555 show that the SKM can reasonably evaluate the first-order response of the problem
556 (i.e., the force-displacement history and tool trajectories). The key behind this
557 modeling success is to capture the evolution of material geometries (e.g., free
558 surface) due to large deformation.

559 The present study has been focused on the evolutionary plasticity processes in-
560 volving Tresca solid (cohesive soil). This cohesive material is selected to simplify
561 the problems such that the key characteristics of the fundamental concept of sim-
562 ulating large deformation processes via SKM can be explored. Specifically, given
563 the incompressibility conditions of cohesive material, the dilation/contraction at
564 velocity discontinuities and the consequent potential material separation/overlay
565 taking place during geometry update can be avoided. On the other hand, it should
566 be noted that the SKM strategy can be applied to the problems dealing with
567 frictional materials, as demonstrated by modeling thrusting sequences in geology
568 (Cubas et al., 2008; Mary et al., 2013) and ploughing sand (Hambleton et al., 2014;
569 Kashizadeh et al., 2015). In these studies, the shear-induced volume change at
570 velocity discontinuities is often neglected when the material geometry is incremen-
571 tally updated, as a means to avoid the aforementioned complications. Therefore,
572 when extending the proposed SKM method to frictional materials, future inves-
573 tigation are needed to explore the methods to update the material geometries in
574 accordance with deformation mechanisms featuring dilation/contraction at veloc-
575 ity jumps.

576 The SKM formulation in this work characterizes material deformation patterns
577 by simple mechanism of rigid elements. This modeling decision reduces the
578 number of unknowns required to constrain optimal velocity fields and consequently
579 leads to relatively efficient simulations. Nevertheless, it should be noted that there

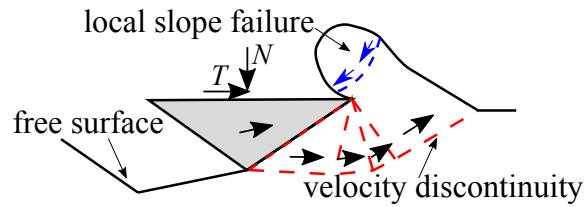


Fig. 20. Schematic illustrating the conditions of overtopping, where material deformation characteristics such as local slope failure cannot be represented by rigid element mechanism.

580 are cases where the aforementioned simple mechanism is not sufficient to fully
 581 characterize material deformation patterns. For instance, when a wedge with finite
 582 size keeps ploughing Tresca solid, the cohesive material at some times might start
 583 to overtop the moving object, as shown in Fig. 20. Under these conditions, local
 584 slope failure of overtopping material might occur, which cannot be represented by
 585 the rigid element mechanism.

586 To accommodate these deformation patterns, the SKM model might need to
 587 employ more sophisticated kinematic mechanisms. They can include deformable
 588 elements and considering material deformation not immediately adjacent to the
 589 object. In the former case, the r -adaptive kinematic method can be modified to
 590 include additional energy dissipation due to element deformation. In the latter case,
 591 a broader material domain might require to be discretized by mesh (e.g., see Kong
 592 (2015) for a detailed discussion on formulating SKM based on finite element limit
 593 analysis). On the other hand, it should be noted that, while more sophisticated
 594 mechanisms can more accurately capture material deformation, they inevitably
 595 increase computation cost. Therefore, the selection of kinematic mechanisms in
 596 the SKM depends on “cost/benefit” considerations done for specific engineering
 597 projects.

598 The response computed by the proposed SKM model strongly relies on the

599 algorithms used to search for an optimal velocity field (i.e., the algorithms used
600 to solve the non-linear optimization of Eq. (7)). A local optimization algorithm is
601 currently employed due to that it is generally more efficient than its global optimiza-
602 tion counterparts. Nevertheless, this type of algorithm might return local optimum
603 and the kinematic mechanism that is not the most critical. As mentioned above,
604 the surface failure mechanism is computed by the SKM when the cylinder has
605 been pushed to relatively deep depths (see Fig. 19(c)). An alternative mechanism,
606 where deformation is confined to the region adjacent to the cylinder (i.e., similar to
607 full-flow mechanism postulated in [Martin and Randolph \(2006\)](#)), can be computed
608 from the current formulation when the optimization solver starts with different
609 initial guesses of nodal positions. This alternative mechanism corresponds to a
610 smaller resistance and thus representing a more critical one. Continuous inves-
611 tigations are required to explore the possibility of resolving this dependence on
612 initial nodal positions without sacrificing computational efficiency, like via global
613 surrogate optimization.

614 In addition to initial nodal positions, the performance of the optimization solver
615 can be sensitive to its controlling parameters, so does the response computed by
616 the SKM model. We use the test 12 performed by [Challen et al. \(1984\)](#) to illustrate
617 this point. It is seen from Fig. 21 that employing a higher value of the parameter T_s
618 (i.e., stop the optimization prematurely) only marginally overestimates the plough-
619 ing force over the first half of the deformation process, but leading to remarkable
620 changes in the computed wedge trajectories and material free surface. The cumu-
621 lative changes in the geometric configurations eventually reach a breakpoint (i.e.,
622 the square symbol in Fig. 21) where the deformation mode fundamentally changes
623 (see the inset of Fig. 21), so does the corresponding ploughing resistance. Future

624 studies can explore the possibility of regularizing the aforementioned dependence
625 of solution on optimization solver parameters, via including deformable elements
626 in kinematic mechanism, as the rigid block assumption might pose overly strong
627 restrictions on available deformation modes.

628 The last limitation of the SKM model observed in this work is that the solution
629 can be sensitive to the presence of irregular shape along the material free surface
630 and thus requiring careful correction of the surface. To illustrate this point, Fig. 22
631 shows the effects of permitting the sharp inverse corner at the free surface. Similar
632 to relaxing the optimization tolerance described above, the irregular shape of the
633 free surface can promote remarkable changes in the computed deformation mode
634 and peculiar jumps in the ploughing forces. This is because the boundary between
635 the moving and stationary materials is trapped at the tip of the inverse angle
636 (see the computed velocity fields in Fig. 22). The issue mentioned above can be
637 addressed by the surface correction scheme discussed in Section 4. However, it
638 should be noted that these correction strategies can violate the conservation of
639 mass, as materials are deleted (for correcting penetration) or added (for correcting
640 the inverse corner). Such induced error can be minimized as relatively small time
641 increments are adopted (see Table 1).

642 **10. Conclusions**

643 This work investigates the potentials of simulating evolutionary plasticity pro-
644 cesses via sequential kinematic method (SKM) constructed on simple deformation
645 mechanism. These processes are modeled by sequentially updating the material
646 geometries in accordance with velocity fields represented by mechanism consist-
647 ing of rigid translational elements separated by velocity discontinuities. Optimal

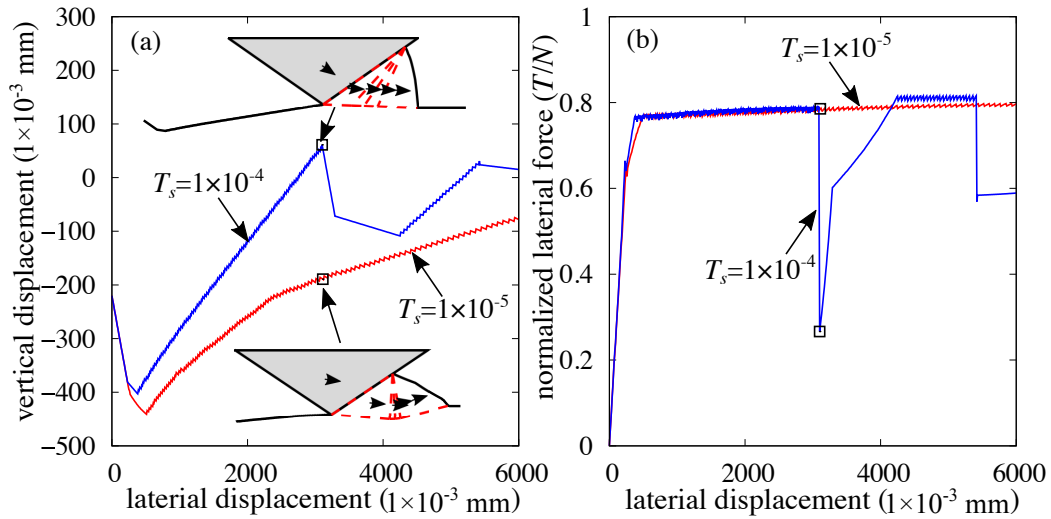


Fig. 21. Influence of the non-linear optimization tolerance T_s on the computed ploughing response.

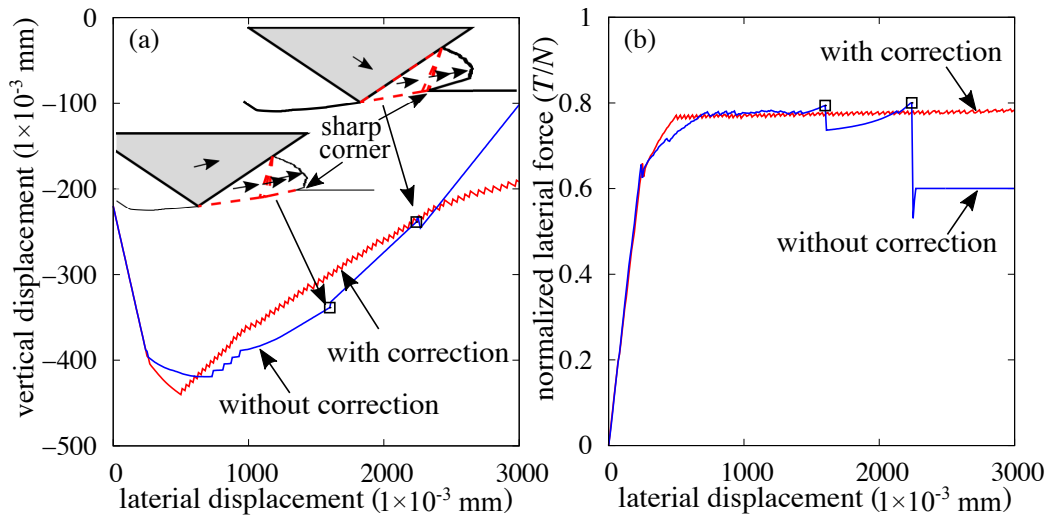


Fig. 22. Influence of the free surface correction on the computed ploughing response.

648 velocity fields are sought by a r -adaptive kinematic method formulation, where
 649 an iterative, nested optimization procedure is constructed that consists of (1) de-
 650 termination of velocities for a fixed mesh of rigid blocks using second-order cone
 651 programming and (2) adaptation of nodal positions using non-linear optimization

652 to find a critical layout of velocity discontinuities. The advantages and limita-
653 tions of the modeling strategy are examined through simulating wedge ploughing
654 Tresca solid and cylinder penetrating undrained clay, where analytical, numerical
655 solutions, and experimental observations are available in the literature. The main
656 conclusions that can be drawn from this work include:

- 657 1. The comparison of the results simulated by using the proposed SKM model
658 against existing solutions and experimental evidence shows that SKM com-
659 bined with conceptually simple deformation mechanism can reasonably rep-
660 resent the first-order response of wedge ploughing and cylinder penetration,
661 including forces and motions of the object.
- 662 2. The proposed SKM technique exhibits promising features for delivering
663 efficient analyses of evolutionary plasticity problems.
- 664 3. The response computed by the SKM depends on spatial and temporal dis-
665 cretization sizes. A converging trend of simulations is seen as the nodal
666 space of the discretized free surface or time increment size becomes smaller.
- 667 4. Both employing a sufficiently small termination tolerance for the non-linear
668 optimization of the nodal positions and appropriately correcting the material
669 free surface can be crucial for obtaining accurate simulations. Without
670 these restrictions, a significant deviation on the objects' trajectories and
671 the material free surface can occur without noticeably altering the computed
672 forces. However, the accumulation of errors in the geometries can eventually
673 lead to large mismatches on the prediction of resistance.

674 In future studies, the proposed SKM model can be extended to the problems
675 dealing with frictional materials. In this aspect, more research efforts might
676 be required focusing on the methods for updating material geometries that can

677 accommodate dilation/contraction at velocity discontinuities. The dependence of
678 kinematic mechanism optimization on initial nodal positions might be resolved
679 by employing efficient global optimization solvers (e.g., surrogate model). The
680 proposed SKM model applies most appropriately if the engineering interest is to
681 quickly evaluate large-deformation plasticity problems to the first order. When
682 the primary interests rest on more accurate representations of soil deformation or
683 detailed response such as the stress and strain fields, the current formulation can
684 be augmented by more sophisticated kinematic mechanisms (e.g., [Kong \(2015\)](#),
685 [Kong et al. \(2018\)](#), [Zhu et al. \(2020\)](#)), or modeling techniques other than SKM can
686 be pursued (e.g., [Agarwal et al. \(2019\)](#), [Afrasiabi et al. \(2019\)](#) and [Recuero et al.
687 \(2017\)](#)).

688 **Acknowledgements**

689 This material is based upon work supported by the National Science Foundation
690 under Grant No. 1846817. This financial support is gratefully acknowledged. The
691 first and second authors acknowledge support provided by the National Natural
692 Science Foundation of China under Grant Nos. 51738010 and 41902278.

693 **References**

- 694 Afrasiabi, M., Roethlin, M., Klippel, H., Wegener, K., 2019. Meshfree simulation
695 of metal cutting: an updated Lagrangian approach with dynamic refinement.
696 *International Journal of Mechanical Sciences* 160, 451–466. doi:[10.1016/j.
697 ijmecsci.2019.06.045](https://doi.org/10.1016/j.ijmecsci.2019.06.045).
- 698 Agarwal, S., Senatore, C., Zhang, T., Kingsbury, M., Iagnemma, K., Goldman,
699 D.I., Kamrin, K., 2019. Modeling of the interaction of rigid wheels with dry

- 700 granular media. *Journal of Terramechanics* 85, 1–14. doi:[10.1016/j.jterra.](https://doi.org/10.1016/j.jterra.2019.06.001)
701 [2019.06.001](https://doi.org/10.1016/j.jterra.2019.06.001).
- 702 Anastasopoulos, I., Gelagoti, F., Kourkoulis, R., Gazetas, G., 2011. Simplified
703 constitutive model for simulation of cyclic response of shallow foundations: Val-
704 idation against laboratory tests. *Journal of Geotechnical and Geoenvironmental*
705 *Engineering* 137, 1154–1168.
- 706 Atkins, T., 2009. *The Science and Engineering of Cutting-The Mechanics and*
707 *Processes of Separating, Scratching and Puncturing Biomaterials, Metals,*
708 *and Non-metals.* Butterworth Heinemann, Oxford, England. doi:[10.1016/](https://doi.org/10.1016/C2009-0-17178-7)
709 [C2009-0-17178-7](https://doi.org/10.1016/C2009-0-17178-7).
- 710 Bil, H., Kiliç, S.E., Tekkaya, A.E., 2004. A comparison of orthogonal cutting
711 data from experiments with three different finite element models. *International*
712 *Journal of Machine Tools and Manufacture* 44, 933–944. doi:[10.1016/j.](https://doi.org/10.1016/j.ijmachtools.2004.01.016)
713 [ijmachtools.2004.01.016](https://doi.org/10.1016/j.ijmachtools.2004.01.016).
- 714 Challen, J.M., McLean, L.J., Oxley, P.L.B., 1984. Plastic deformation of a metal
715 surface in sliding contact with a hard wedge: Its relation to friction and wear.
716 *Proceedings of the Royal Society A: Mathematical, Physical and Engineering*
717 *Sciences* 394, 161–181. doi:[10.1098/rspa.1984.0074](https://doi.org/10.1098/rspa.1984.0074).
- 718 Challen, J.M., Oxley, P.L., 1979. An explanation of the different regimes of friction
719 and wear using asperity deformation models. *Wear* 53, 229–243. doi:[10.1016/](https://doi.org/10.1016/0043-1648(79)90080-2)
720 [0043-1648\(79\)90080-2](https://doi.org/10.1016/0043-1648(79)90080-2).
- 721 Chen, W.F., 1975. *Limit Analysis and Soil Plasticity.* Elsevier Scientific Publishing
722 Company, Amsterdam, The Netherlands.

- 723 Collins, I.F., 1972. A simplified analysis of the rolling of a cylinder on a
724 rigid/perfectly plastic half-space. *International Journal of Mechanical Sciences*
725 14, 1–14. doi:[10.1016/0020-7403\(72\)90002-1](https://doi.org/10.1016/0020-7403(72)90002-1).
- 726 Corradi, L., Panzeri, N., 2004. A triangular finite element for sequential limit
727 analysis of shells. *Advances in Engineering Software* 35, 633–643. doi:[10.](https://doi.org/10.1016/j.advengsoft.2004.03.014)
728 [1016/j.advengsoft.2004.03.014](https://doi.org/10.1016/j.advengsoft.2004.03.014).
- 729 Cubas, N., Leroy, Y.M., Maillot, B., 2008. Prediction of thrusting sequences
730 in accretionary wedges. *Journal of Geophysical Research: Solid Earth* 113,
731 B12412. doi:[10.1029/2008JB005717](https://doi.org/10.1029/2008JB005717).
- 732 Dayal, U., Allen, J.H., 1975. The effect of penetration rate on the strength of
733 remolded clay and sand samples. *Canadian Geotechnical Journal* 12, 336–348.
- 734 De Vathaire, M., Delamare, F., Felder, E., 1981. An upper bound model of plough-
735 ing by a pyramidal indenter. *Wear* 66, 55–64. doi:[10.1016/0043-1648\(81\)](https://doi.org/10.1016/0043-1648(81)90032-6)
736 [90032-6](https://doi.org/10.1016/0043-1648(81)90032-6).
- 737 Drucker, D.C., Prager, W., Greenberg, H.J., 1952. Extended limit design theorems
738 for continuous media. *Quarterly of Applied Mathematics* 9, 381–389. doi:[10.](https://doi.org/10.1090/qam/45573)
739 [1090/qam/45573](https://doi.org/10.1090/qam/45573).
- 740 Ducobu, F., Rivière-Lorphèvre, E., Filippi, E., 2016. Application of the Cou-
741 pled Eulerian-Lagrangian (CEL) method to the modeling of orthogonal cut-
742 ting. *European Journal of Mechanics, A/Solids* 59, 58–66. doi:[10.1016/j.](https://doi.org/10.1016/j.euromechsol.2016.03.008)
743 [euromechsol.2016.03.008](https://doi.org/10.1016/j.euromechsol.2016.03.008).

- 744 Einav, I., Randolph, M.F., 2005. Combining upper bound and strain path meth-
745 ods for evaluating penetration resistance. *International Journal for Numerical*
746 *Methods in Engineering* 63, 1991–2016.
- 747 Godwin, R.J., O’Dogherty, M.J., 2007. Integrated soil tillage force prediction
748 models. *Journal of Terramechanics* 44, 3–14.
- 749 Hambleton, J.P., 2010. Plastic analysis of processes involving material-object
750 interaction. Ph.D. thesis. The University of Minesota. Minneapolis and Saint
751 Paul, United States.
- 752 Hambleton, J.P., Drescher, A., 2009. On modeling a rolling wheel in the presence
753 of plastic deformation as a three- or two-dimensional process. *International*
754 *Journal of Mechanical Sciences* 51, 846–855. doi:[10.1016/j.ijmecsci.](https://doi.org/10.1016/j.ijmecsci.2009.09.024)
755 [2009.09.024](https://doi.org/10.1016/j.ijmecsci.2009.09.024).
- 756 Hambleton, J.P., Drescher, A., 2012. Approximate model for blunt objects in-
757 denting cohesive-frictional materials. *International Journal for Numerical and*
758 *Analytical Methods in Geomechanics* 36, 249–271. doi:[10.1002/nag.1004](https://doi.org/10.1002/nag.1004).
- 759 Hambleton, J.P., Sloan, S.W., 2013. A perturbation method for optimization of
760 rigid block mechanisms in the kinematic method of limit analysis. *Computers*
761 *and Geotechnics* 48, 260–271. doi:[10.1016/j.compgeo.2012.07.012](https://doi.org/10.1016/j.compgeo.2012.07.012).
- 762 Hambleton, J.P., Stanier, S.A., White, D.J., Sloan, S.W., 2014. Modelling plough-
763 ing and cutting processes in soils. *Australian Geomechanics* 49, 147–156.
- 764 Herfelt, M.A., Krabbenhøft, J., Krabbenhøft, K., 2021. Modelling of ‘no-tension’
765 interfaces. *Computers and Geotechnics* 129, 103860.

- 766 Hettiaratchi, D., Reece, A., 1974. The calculation of passive soil resistance.
767 *Géotechnique* 24, 289–310.
- 768 Hill, R., 1950. *The Mathematical Theory of Plasticity*. Oxford University Press.
- 769 Hill, R., Lee, E., Tupper, S., 1947. The theory of wedge indentation of ductile
770 materials. *Proceedings of the Royal Society of London. Series A. Mathematical*
771 *and Physical Sciences* 188, 273–289. doi:[10.1098/rspa.1947.0009](https://doi.org/10.1098/rspa.1947.0009).
- 772 Houlsby, G.T., Puzrin, A.M., 1999. The bearing capacity of a strip footing on clay
773 under combined loading. *Proceedings of the Royal Society of London. Series*
774 *A: Mathematical, Physical and Engineering Sciences* 455, 893–916.
- 775 Hryciw, R.D., Raschke, S.A., Ghalib, A.M., Horner, D.A., Peters, J.F., 1997.
776 Video tracking for experimental validation of discrete element simulations of
777 large discontinuous deformations. *Computers and Geotechnics* 21, 235–253.
778 doi:[10.1016/s0266-352x\(97\)00014-1](https://doi.org/10.1016/s0266-352x(97)00014-1).
- 779 Hwan, C.L., 1997. Plane strain extrusion by sequential limit analysis. *International*
780 *Journal of Mechanical Sciences* 39, 807–817. doi:[10.1016/s0020-7403\(96\)](https://doi.org/10.1016/s0020-7403(96)00089-6)
781 [00089-6](https://doi.org/10.1016/s0020-7403(96)00089-6).
- 782 Johnson, D., 1995. Yield-line analysis by sequential linear programming. *In-*
783 *ternational Journal of Solids and Structures* 32, 1395–1404. doi:[10.1016/](https://doi.org/10.1016/0020-7683(94)00200-G)
784 [0020-7683\(94\)00200-G](https://doi.org/10.1016/0020-7683(94)00200-G).
- 785 Karapiperis, K., Gerolymos, N., 2014. Combined loading of caisson foundations
786 in cohesive soil: Finite element versus Winkler modeling. *Computers and*
787 *Geotechnics* 56, 100–120.

- 788 Kashizadeh, E., 2017. Theoretical and Experimental Analysis of the Cutting
789 Process in Sand. Master's thesis. The University of Newcastle. Callaghan,
790 Australia.
- 791 Kashizadeh, E., Hambleton, J.P., Stanier, S.A., 2015. A numerical approach for
792 modelling the ploughing process in sands, in: Analytical Methods in Petroleum
793 Upstream Applications, CRC Press. pp. 159–164.
- 794 Kong, D., 2015. Large displacement numerical analysis of offshore pipe-soil
795 interaction on clay. Ph.D. thesis. University of Oxford. Oxford, England.
- 796 Kong, D., Martin, C., Byrne, B., 2017. Modelling large plastic deformations of co-
797 hesive soils using sequential limit analysis. International Journal for Numerical
798 and Analytical Methods in Geomechanics 41, 1781–1806.
- 799 Kong, D., Martin, C.M., Byrne, B.W., 2018. Sequential limit analysis of pipe–soil
800 interaction during large-amplitude cyclic lateral displacements. Géotechnique
801 68, 64–75. doi:[10.1680/jgeot.16.p.256](https://doi.org/10.1680/jgeot.16.p.256).
- 802 Ladd, C.C., Foott, R., 1974. New design procedure for stability of soft clays.
803 Journal of the Geotechnical Engineering Division 100, 763–786.
- 804 Lemaitre, J., Chaboche, J.L., 1990. Mechanics of Solid Materials. Cambridge
805 University Press, New York.
- 806 Leon Bal, A.R., Hoppe, U., Dang, T.S., Hackl, K., Meschke, G., 2018. Hypoplas-
807 tic particle finite element model for cutting tool-soil interaction simulations:
808 Numerical analysis and experimental validation. Underground Space 3, 61–71.
809 doi:[10.1016/j.undsp.2018.01.008](https://doi.org/10.1016/j.undsp.2018.01.008).

- 810 Li, C., Zhang, T., Goldman, D.I., 2013. A terradynamics of legged locomotion on
811 granular media. *Science* 339, 1408–1412. doi:[10.1126/science.1229163](https://doi.org/10.1126/science.1229163),
812 [arXiv:1303.7065](https://arxiv.org/abs/1303.7065).
- 813 Martin, C., Randolph, M., 2006. Upper-bound analysis of lateral pile capacity in
814 cohesive soil. *Géotechnique* 56, 141–145.
- 815 Mary, B.C.L., Maillot, B., Leroy, Y.M., 2013. Deterministic chaos in frictional
816 wedges revealed by convergence analysis. *International Journal for Numerical
817 and Analytical Methods in Geomechanics* 37, 3036–3051.
- 818 McKyes, E., 1985. *Soil cutting and tillage*. Elsevier Scientific Publisher B. V., Am-
819 sterdam, The Netherlands. doi:[10.1016/B978-0-444-88080-2.50013-2](https://doi.org/10.1016/B978-0-444-88080-2.50013-2).
- 820 Milani, G., Lourenço, P.B., 2009. A discontinuous quasi-upper bound limit anal-
821 ysis approach with sequential linear programming mesh adaptation. *Internation-
822 al Journal of Mechanical Sciences* 51, 89–104. doi:[10.1016/j.ijmecsci.
823 2008.10.010](https://doi.org/10.1016/j.ijmecsci.2008.10.010).
- 824 Mosek, 2015. *The MOSEK optimization toolbox for MATLAB*. MOSEK ApS.
- 825 Mroz, Z., 1967. On the description of anisotropic workhardening. *Journal of the
826 Mechanics and Physics of Solids* 15, 163–175.
- 827 Osman, M.S., 1964. The mechanics of soil cutting blades. *Journal of Agricultural
828 Engineering Research* 9, 313–328.
- 829 Palmer, A., 1999. Speed effects in cutting and ploughing. *Géotechnique* 49,
830 285–294.

- 831 Perumpral, J.V., Grisso, R.D., Desai, C.S., 1983. A soil-tool model based on
832 limit equilibrium analysis. Transactions of the ASAE 26, 0991–0995. doi:[10.
833 13031/2013.34062](https://doi.org/10.13031/2013.34062).
- 834 Petryk, H., 1980. Non-unique slip-line field solutions for the wedge indentation
835 problem. Journal de Mécanique appliquée 4, 255–282.
- 836 Petryk, H., 1983. A slip-line field analysis of the rolling contact problem at high
837 loads. International Journal of Mechanical Sciences 25, 265–275. doi:[10.
838 1016/0020-7403\(83\)90030-9](https://doi.org/10.1016/0020-7403(83)90030-9).
- 839 Prandtl, L., 1920. Über die härte plastischer körper. Nachr. K. Ges. Wiss. Göttin-
840 gen., Math. Phys. Klasse , 74–85.
- 841 Prévost, J., 1977. Mathematical modelling of monotonic and cyclic undrained
842 clay behaviour. International Journal for Numerical and Analytical Methods in
843 Geomechanics 1, 192–216.
- 844 Raithatha, A., Duncan, S.R., 2009. Rigid plastic model of incremental sheet
845 deformation using second-order cone programming. International Journal for
846 Numerical Methods in Engineering 78, 955–979. doi:[10.1002/nme.2512](https://doi.org/10.1002/nme.2512).
- 847 Randolph, M.F., 2004. Characterization of soft sediments for offshore applications,
848 keynote lecture, in: Proc. Second International Conference on Geotechnical and
849 Geophysical Site Characterization.
- 850 Randolph, M.F., Houlsby, G.T., 1984. The limiting pressure on a circular pile
851 loaded laterally in cohesive soil. Géotechnique 34, 613–623.

- 852 Recuero, A., Serban, R., Peterson, B., Sugiyama, H., Jayakumar, P., Negrut, D.,
853 2017. A high-fidelity approach for vehicle mobility simulation: Nonlinear finite
854 element tires operating on granular material. *Journal of Terramechanics* 72,
855 39–54. doi:[10.1016/j.jterra.2017.04.002](https://doi.org/10.1016/j.jterra.2017.04.002).
- 856 Shi, Z., Hambleton, J.P., 2020. An r-h adaptive kinematic approach for 3D limit
857 analysis. *Computers and Geotechnics* 124, 103531.
- 858 Stanier, S.A., White, D.J., 2013. Improved image-based deformation measurement
859 in the centrifuge environment. *Geotechnical Testing Journal* 36, 1–14. doi:[10.1520/GTJ20130044](https://doi.org/10.1520/GTJ20130044).
- 860
- 861 Sturm, J.F., 2002. Implementation of interior point methods for mixed semidefi-
862 nite and second order cone optimization problems. *Optimization Methods and*
863 *Software* 17, 1105–1154. doi:[10.1080/1055678021000045123](https://doi.org/10.1080/1055678021000045123).
- 864 Tabor, D., 1959. Junction growth in metallic friction: the role of combined stresses
865 and surface contamination. *Proceedings of the Royal Society of London. Series*
866 *A. Mathematical and Physical Sciences* 251, 378–393. doi:[10.1098/rspa.](https://doi.org/10.1098/rspa.1959.0114)
867 [1959.0114](https://doi.org/10.1098/rspa.1959.0114).
- 868 Terzaghi, K., 1943. *Theoretical Soil Mechanics*. John Wiley and Sons.
- 869 Tian, Y., Cassidy, M.J., 2010. The challenge of numerically implementing numer-
870 ous force-resultant models in the stability analysis of long on-bottom pipelines.
871 *Computers and Geotechnics* 37, 216–232. doi:[10.1016/j.compgeo.2009.](https://doi.org/10.1016/j.compgeo.2009.09.004)
872 [09.004](https://doi.org/10.1016/j.compgeo.2009.09.004).
- 873 Tsuji, T., Nakagawa, Y., Matsumoto, N., Kadono, Y., Takayama, T., Tanaka, T.,
874 2012. 3-D DEM simulation of cohesive soil-pushing behavior by bulldozer

- 875 blade. *Journal of Terramechanics* 49, 37–47. doi:[10.1016/j.jterra.2011.](https://doi.org/10.1016/j.jterra.2011.11.003)
876 [11.003](https://doi.org/10.1016/j.jterra.2011.11.003).
- 877 White, D., Dingle, H., 2011. The mechanism of steady friction between seabed
878 pipelines and clay soils. *Géotechnique* 61, 1035–1041. doi:[10.1680/geot.8.](https://doi.org/10.1680/geot.8.t.036)
879 [t.036](https://doi.org/10.1680/geot.8.t.036).
- 880 White, D.J., Take, W.A., 2002. GeoPIV: Particle Image Velocimetry (PIV) soft-
881 ware for use in geotechnical testing. Technical Report CUED/D-SOILS/TR322.
882 Cambridge University, Engineering Department. Cambridge, United Kingdom.
883 doi:[10.7710/1093-7374.1624](https://doi.org/10.7710/1093-7374.1624).
- 884 Xu, W., Zhang, L., 2019. Heat effect on the material removal in the machining
885 of fibre-reinforced polymer composites. *International Journal of Machine Tools*
886 *and Manufacture* 140, 1–11. doi:[10.1016/j.ijmachtools.2019.01.005](https://doi.org/10.1016/j.ijmachtools.2019.01.005).
- 887 Yang, W.H., 1993. Large deformation of structures by sequential limit analysis.
888 *International Journal of Solids and Structures* 30, 1001–1013.
- 889 Zhang, X., Krabbenhoft, K., Sheng, D., Li, W., 2015. Numerical simulation of
890 a flow-like landslide using the particle finite element method. *Computational*
891 *Mechanics* 55, 167–177.
- 892 Zhang, X., Wang, L., Krabbenhoft, K., Tinti, S., 2020. A case study and impli-
893 cation: particle finite element modelling of the 2010 Saint-Jude sensitive clay
894 landslide. *Landslides* , 1–11.
- 895 Zhu, B., Dai, J., Kong, D., 2020. Modelling T-bar penetration in soft clay us-
896 ing large-displacement sequential limit analysis. *Géotechnique* 70, 173–180.
897 doi:[10.1680/jgeot.18.p.160](https://doi.org/10.1680/jgeot.18.p.160).